

Afar triple junction fed by single, heterogeneous mantle upwelling

Emma J. Watts and et al.

^{1*}School of Ocean & Earth Science, University of Southampton,
European Way, Southampton, SO14 3ZH, UK.

*Corresponding author(s). E-mail(s): e.j.watts@soton.ac.uk;
Contributing authors: iiauthor@gmail.com;

Abstract

Volcanism is associated with plate tectonics or the arrival of hot upwellings, known as mantle plumes, from Earth's deep interior (1; 2). Plumes are thought to play a crucial role in continental breakup and the formation of ocean basins [3], yet many aspects of their influence remain enigmatic. A classic case study, the Afar triple junction in East Africa, comprises three rifts at varying stages of evolution and has been proposed to be underlain by a mantle plume (4; 5); however, others argue for limited plume involvement [6]. We present extensive geochemical and isotopic data spanning the region and integrate these with existing geochemical and geophysical datasets to identify a first-order plume influence on both the composition, and abundance, of melt. Here we show that the mantle beneath Afar can be best explained by the presence of a single, asymmetric heterogeneous mantle plume. In each rift arm we identify variations in mantle compositions on characteristic length scales (50-150 km), which is longer in the more evolved and faster rifting sectors suggesting more rapid channelised flow. Our results demonstrate that mantle upwellings can be heterogeneous, supporting previous suggestions (7; 8; 9), and heavily influenced by the dynamics of the overriding plates. Our approach highlights the potential of combining geochemistry, geophysics and modelling to gain valuable insights into the spatially complex characteristics of mantle upwellings.

1 Introduction

The role of hotspots or mantle plumes in driving volcanism during continental breakup has long been debated, but with only a small fraction of Earth’s mantle plumes situated under continents [10] and a limited number of plumes associated with active continental rifting [11], our understanding of these processes remains incomplete. In the ‘classic’ magma assisted continental rift, the Afar triple junction—where the Arabian, African, and Somali tectonic plates intersect—all three rifts are currently active [12], making it an ideal location to study the interactions between mantle upwelling and continental rifts. Here, the driver of melt production is debated with some models suggesting decompression melting with minimal plume involvement [6], while others propose scenarios involving upwelling of hot, deep mantle [13], or plumes (14; 15). Several discrete segments of the rift have been studied in terms of magma petrogenesis (e.g., 13; 16). However, a paucity of high-precision geochemical data across the broader region hampers our ability to test the above models and evaluate the spatial characteristics and structure of this major mantle upwelling in the recent geologic past.

2 Investigating the Presence of a Plume

To overcome this significant limitation, we begin our study by implementing the most comprehensive and spatially representative sampling strategy, focusing on younger volcanoes that span all three rift systems. Our sampling specifically targets rocks that are Quaternary in age, less than 2.58 million years (Myr) old, and from volcanoes that have been active during the Holocene period, which began 11.7 thousand years ago (ka) [17]. By targeting younger rocks, we aim to make a direct comparison with geophysical data across the entire region, enabling an unprecedented multidisciplinary investigation of mantle petrogenesis and dynamics.

Our new data compilation includes over 150 rock samples, more than doubling the number of high-quality analyses in the area, with many from previously unstudied volcanoes. These samples were carefully selected from a repository covering the broader Afar region (see Section 5 for further details), supplemented by additional samples collected during fieldwork in the Main Ethiopian Rift (MER). All samples were analysed for major and trace elements and radiogenic isotopes (see Section 5) to quantify the spatial trends in the geochemistry of surface volcanism. We also integrate high-quality data from the open-source GEOROC data repository (<https://georoc.eu/>; 20) for rocks, including the classic catalogue from [15] (i.e., the Gulf of Aden), where a complete set of analyses was available within the area of interest (see Section 5). Additionally, we leverage recent spatial maps of key geophysical variables, such as the depth of the Mohorovičić discontinuity (see Section 5 for further details) and shear wave velocities at various depths (40, 80, and 120 km; 21). These variables provide well-established proxies for the boundary between the crust and mantle, as well as for the presence and abundance of melt within the lithosphere and asthenosphere [21]. Collectively, this information allows us to build an unprecedented picture of the depth, extent, and compositional characteristics of melts distributed spatially across all three rifts.

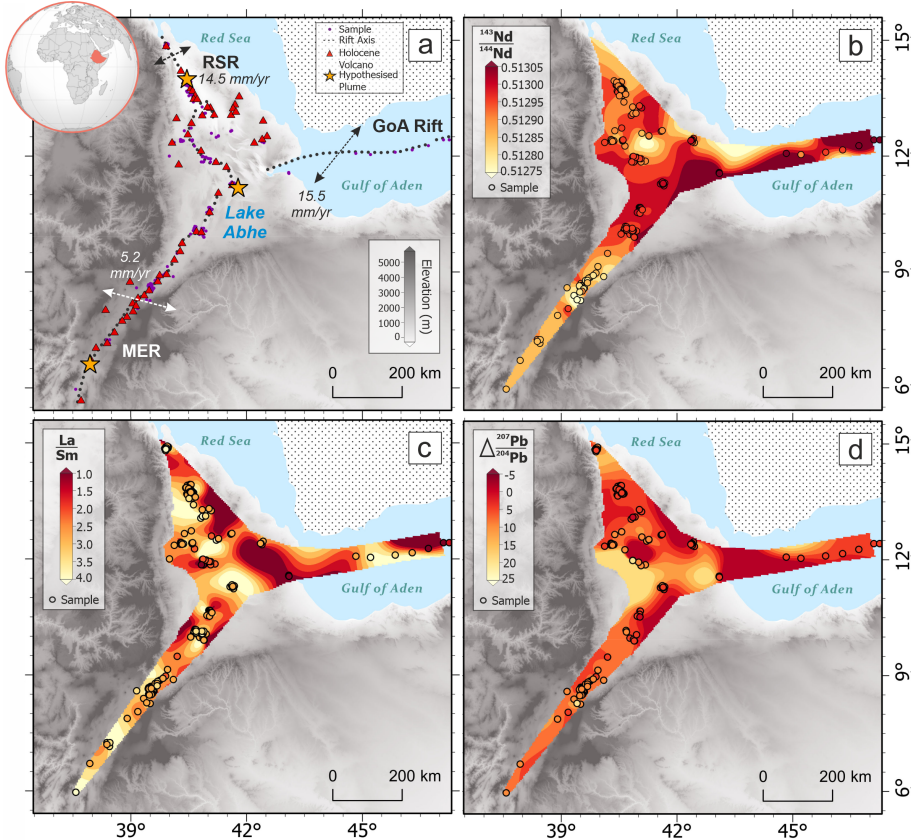


Fig. 1 (a) Map showing the three rifts: Gulf of Aden (GoA) Rift, Red Sea Rift (RSR) and the Main Ethiopian Rift (MER) shown by a dashed line and the rifts associated rifting rates (after 18 & 19). The three suspected plume locations (yellow stars), Holocene volcanoes (red triangles) and sample locations (purple dots) are all shown. (b) Interpolated map showing the $^{143}\text{Nd}/^{144}\text{Nd}$ variations across the study region (red = high plume-like $^{143}\text{Nd}/^{144}\text{Nd}$, yellow = low $^{143}\text{Nd}/^{144}\text{Nd}$). Sample locations are shown by circles and their associated $^{143}\text{Nd}/^{144}\text{Nd}$ values indicated by colour fill. (c) Interpolated map showing the La/Sm variations across the study region (red = low La/Sm – high melt fraction, yellow = high La/Sm – low melt fraction). Sample locations are shown by circles and their associated variable values indicated by colour fill. (d) Interpolated map showing the $^{87}\text{Sr}/^{86}\text{Sr}$ variations across the study region (red = low plume-plume $^{207}\text{Pb}/^{204}\text{Pb}$, yellow = high $^{206}\text{Pb}/^{204}\text{Pb}$). Sample locations are shown by circles and their associated values indicated by colour fill.

Mantle plumes, widely accepted to tap a deep-mantle component called C (common; 22) and/or FOZO (focus zone; 23), have an isotopically distinct composition (i.e., generally low $^{87}\text{Sr}/^{86}\text{Sr}$, high $^{143}\text{Nd}/^{144}\text{Nd}$, and high $^{206}\text{Pb}/^{204}\text{Pb}$; 23), elevated trace element ratios ($\Delta\text{Nb} > 0$, see Eq. ??; 24; Ce/Pb > 30), and are commonly associated with reduced seismic velocities (Vs, Vp) (25; 26). We find that all samples within our study region, that is, within 500 km of the Afar triple junction, exhibit strong C/FOZO signatures (Figs. 1 & Extended Fig. A1), supporting a first-order plume control on the composition and abundance of melt (27; 26; 15). When we apply a spline interpolation of the data (see Section 5), we detect prominent isotopic and geochemical variations

across the broader region (Fig. 1). This includes distinctly elevated La/Sm, Ce/Pb, and $^{206}\text{Pb}/^{204}\text{Pb}$, and decreased $^{87}\text{Sr}/^{86}\text{Sr}$ and shear wave speeds in northern Afar, central Afar (near the triple junction), and sporadically along the MER and Gulf of Aden Rift (Figs. 1 & Extended Fig. A1). These spatial trends implicate an underlying complexity to magmatism and mantle upwelling, which has been detected using geophysical approaches (e.g., 28; 21; 29; 30).

These data and observations enable rigorous testing of plume models. The first model we consider is a simple, homogeneous mantle plume impinging at the triple junction (e.g., 15), which is expected to produce a systematic shift in plume indicator variables radially with distance (Fig. 2). Extending this model, we then allow the plume to be spatially and temporally heterogeneous, as reported in Hawaiian [31] and Canary Island [9] volcanoes. This mechanism would yield a similar pattern to the first model centred at the triple junction, but accommodate compositional fluctuations over the radial distance corresponding to the arrival of chemically distinct pulses (Fig. 2).

We additionally test whether the spatial variations observed (Figs. 1 & Extended Fig. A1) are best explained through the presence of numerous small-scale plumes, or plumelets, which have been proposed based on geophysics and numerical models [29]. Using our spline-interpolated maps (Figs. 1 & Extended Fig. A1), we test this model using three plumelets, one centred on the triple junction, one in the Danakil depression in the north of the Afar region, and one in the southern MER, with the positions of these loci informed by observations (see Section 5).

The strong mantle signatures observed across the wider area (Figs. 1 & Extended Fig. A1b) generally suggest that crustal assimilation has played a relatively minor role in recent magmatism. This finding is consistent with geochemical and isotope evidence, indicating that crustal assimilation was much more significant during earlier stages of rifting, at approximately 30 Ma, when the continental crust was thicker and magmatic fluxes were higher [32]. In contrast, the current crust is heavily thinned and has been intruded by mafic melts along the length of the rift axes. Seismic analysis indicates that recent magmatic activity beneath the rift axis in Afar is transient [33] and, in turn, that magmas are unlikely to reside in crustal reservoirs for long enough to assimilate crustal lithologies.

To interrogate this further, we explore the correlation between key indicators (Fig. 3b) and the depth to the Moho, as crustal thickness likely influences the degree of assimilation [32; see Section 5]. We found that most indicators, including Pb isotopes — a reliable indicator for crustal assimilation [34] — exhibit only weak correlation (Pearson correlation coefficient <0.5) with the Moho depth (Fig. 3b). On the other hand, Ce/Pb exhibits a strong negative correlation (Pearson correlation coefficient of -0.7), indicating that when the crustal thickness is thin, the Ce/Pb value is high, and vice versa. This trend can be attributed to minimal crustal assimilation across most of the region, but with a slight increase as the crust thickens within the MER. Nevertheless, we can test this further by excluding several outliers ($n=94$) where Ce/Pb values fall below 20, as these cases could feasibly be tied to local crustal assimilation [34].

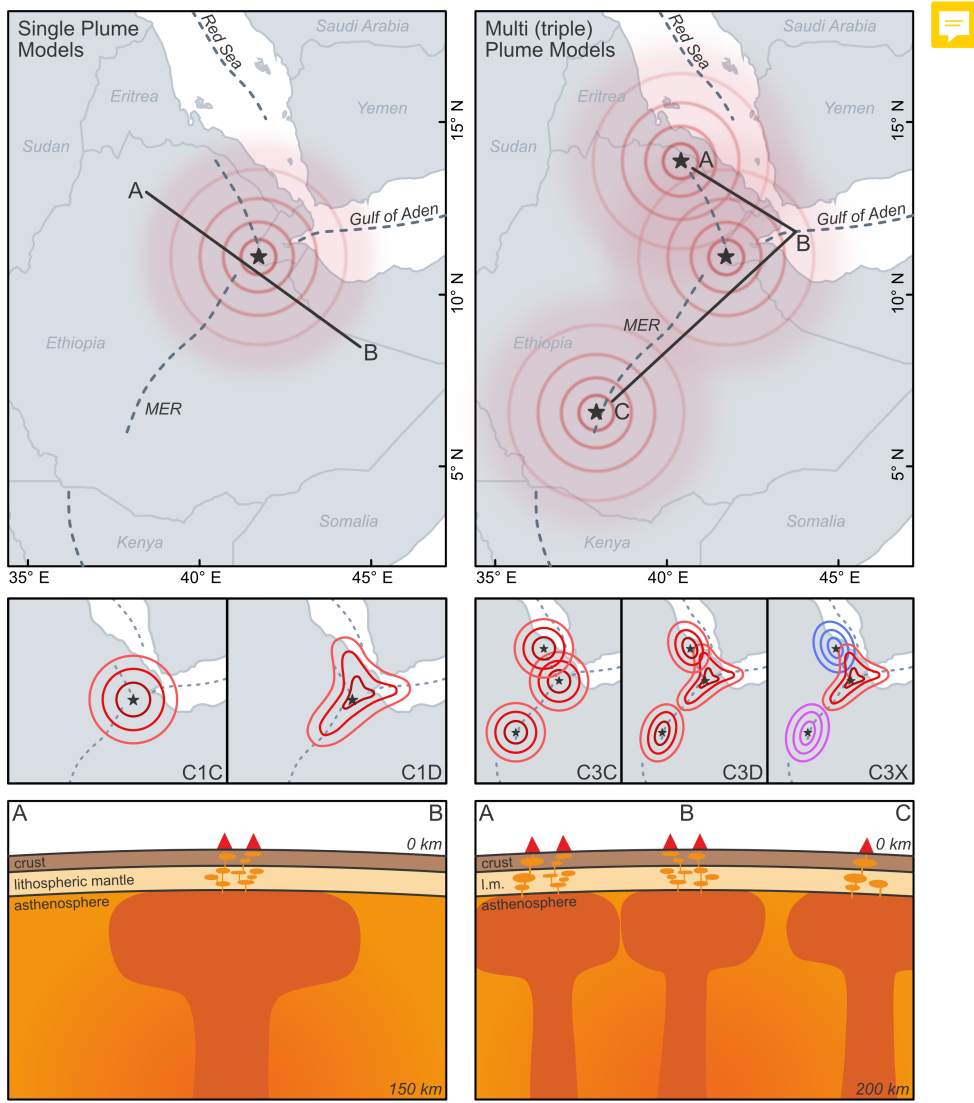


Fig. 2 Schematic diagram of the plume theories for Afar that were tested within this study. The diagrams are labelled with the code associated with each model (see Table 1 for further details). Left: singular plume model, with the variations of the model (i.e., C1C, C1D) shown below. Right: plumelet model testing three plumelets. The variations for each model (i.e., C3C, C3D & C3X) shown below.

3 Afar Plume's Spatial Characteristics

To test between a singular plume (hereafter referred to as model 'C1C') and plumelets (model 'C3C'), we identify eleven key geochemical and geophysical variables (see Extended Table A1) and calculate the distance, using the spherical cosine law (see Section 5.2 for Eq. 5), between the proposed plume centre (35; 5; 15) and each individual observation site (see Section 5). We then apply two-deep cross validation to find

the optimum linear fit (i.e., representing a homogeneous plume) and penalised B-spline fit (i.e., representing a heterogeneous plume) to each of the variables over a radial distance of 500 km, the radial limit of data points considered within this study (Figs. 3c & A2). The predictive performance of each fit is then assessed by calculating the mean standardised root-mean squared error of prediction (RMSEP; Fig. 3a), where a value of 1 shows a lack of predictive capability, and 0 a perfect predictive ability. For both models (C3C and C1C) we observe the B-spline fit (that is, a [class of polynomial functions](#)) to have the best predictive performance, compared to a linear fit. This indicates that a compositionally heterogeneous plume is most likely (Figs. 3a & 3c). However, [minimal](#) differences in predictive performance are observed between the single plume model (C1C; RMSEP = 0.75) versus the plumelets model (C3C; RMSEP = 0.73), assuming the distribution with distance is symmetrical across all rifts.

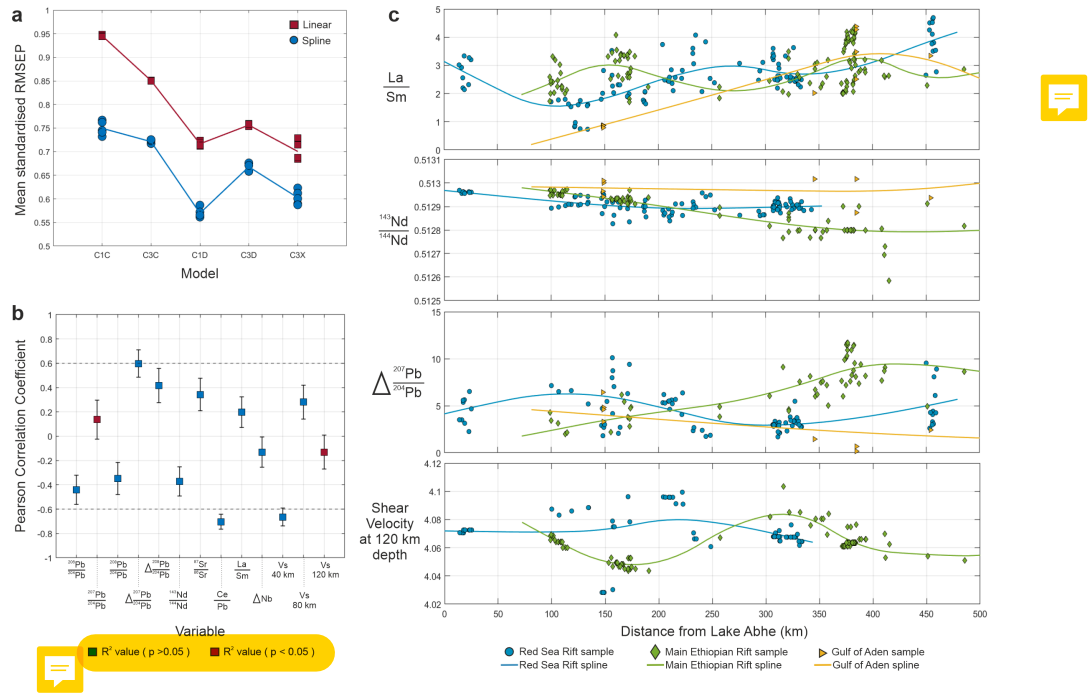


Fig. 3 (a) The mean standardised root mean square error of prediction (RMSEP) for each of the models tested (described in Section 5). Individual linear model results are shown by red squares and the mean of those results are displayed by the red line. Individual spline results are shown by blue circles and the mean of those results are shown by a blue line. (b) Pearson correlation coefficient of each of the selected 11 variables (see Section 5 for details) with Moho depth. Error bars show the 95-percentile error of the coefficient. Blue squares indicate where the correlation is significant ($p < 0.05$) and red squares indicate that the correlations are not deemed significant ($p > 0.05$). (c) Splines (lines) of the winning model (C1C) for selected variables. Symbols show the data within the study (blue circles = Red Sea Rift, green diamonds = Main Ethiopian Rift, yellow triangles = Gulf of Aden Rift).

It is possible that variable extension rates between the three rift systems [12] introduces further complexity to the geochemical and geophysical signals. Accordingly, we introduce three further models, C1D, C3D, and C3X (Fig. 3a; see Section 5 for details) to investigate how regional factors may influence plume behaviour. Models C1D and C3D consider one plume and three plumelets, respectively, while allowing for distinct distance-dependent patterns for each rift, thereby modelling the distribution of each rift independently. Unlike the other models, C3X allows each plumelet to have a distinct signature, as well as permitting independent distribution along each rift (see Section 5 for details). We then obtain the optimum linear and B-spline fit for these three models (C1D, C3D, C3X). This statistical analysis indicates that the overall best predictive model is the B-spline fit of C1D — where a single, heterogeneous mantle plume is present, yet the distribution of key variables (Extended Table A1) differs between rift-arms—which yields a mean standardised RMSEP of 0.58 (Fig. 3a). Our analysis (see Section 5 for details), when excluding $\text{Ce}/\text{Pb} < 20$, reveals that excluding such cases does not affect our overall results (Fig. A7), suggesting that mantle plume variations exert primary control over magma compositions. While the rifts share a common compositionally heterogeneous plume upwelling, they essentially behave independently implying that some feature of their tectonic regime may modulate the observed signals.

4 Interplay Between Plume and Segmentation

We find that many of the optimum splines for each rift display distance-dependent sinusoidal-like patterns (Figs. 3c & A2). Importantly, our analysis indicates that the variability observed for some indicators within the MER are of greater amplitude and shorter periodicity with distance compared to those of the Red Sea Rift and Gulf of Aden Rift (Figs. 3c & A2). Further, the observed variation in Pb isotopes suggests that the plume may be chemically heterogeneous across some elements, but more homogenous in terms of $^{87}\text{Sr}/^{86}\text{Sr}$ and $^{143}\text{Nd}/^{144}\text{Nd}$. Although the broadly consistent positive ΔNb values suggest a first-order plume control across the region, we can identify small-scale differences in La/Sm and Vs velocity at 120 km depth (within the melt zone in the asthenosphere; 36) with distance in each rift (Figs. 3c & A2), which likely indicates locally variable degrees of melting across the region. This raises the question: do the zones of locally higher melt fraction and variable isotopic compositions observed in one rift correspond to those observed in the other rifts?

To address this question, we carried out principal component analysis (PCA) and K-mean cluster analysis using all variables post-standardisation. Across all variables, the K-means cluster analysis algorithm seeks to group similar observations whilst minimising the within-cluster total sum of squares for a pre-specified number of clusters. Our results from K-means cluster analysis (Extended Fig. A3; see Section 5 for details), show a higher number of clusters, smaller in geographic size, assigned to the MER compared to the Red Sea Rift. Several clusters are found to co-occur in different rift-arms. For example, samples assigned to cluster 1 are observed in the distal section of Red Sea Rift, as well as in locations closer to the rift centre within the MER (Extended Fig. A4). This compositional similarity may indicate that they are derived



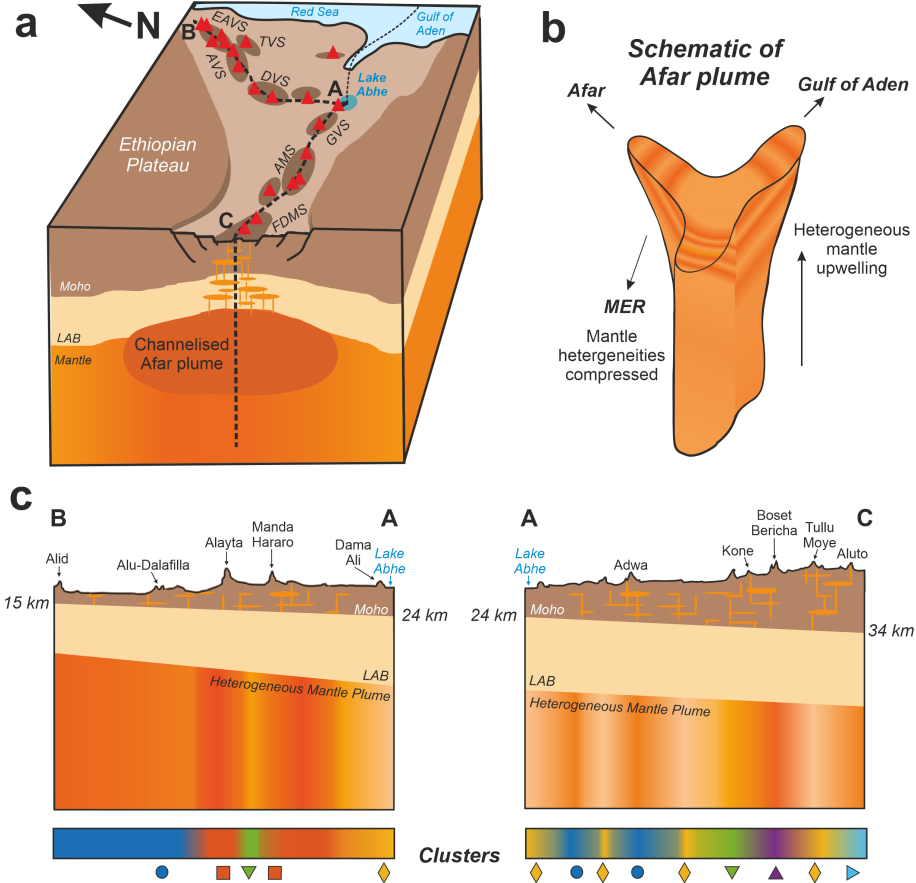


Fig. 4 Schematic of the characteristics of the Afar plume. (a) Box diagram showing the rifts across Afar and the mantle plume being channelised by the rift. The lines of section A-B-C are those drawn in (c). (b) Schematic of the Afar plume showing the dimensions as a result of channelised flow along the rifts. (c) Cross sections along the Red Sea Rift (A-B) and MER (A-C) showing the distribution of mantle heterogeneities and how that links to the clusters shown in Figure A4.

from the same parent melt, although the distribution of these melts within the MER appears to be more condensed over shorter distances compared to the Red Sea Rift.

The spatial distribution of these clusters reflect variations in composition and abundance of melt (Extended Fig. A4). The spatial distribution of the clusters shares some cursory similarities to the magmatic segments (Extended Fig. A4). However, when inspected in detail we observe clear differences. For example, volcanic systems both within magmatic segments and adjacent rift flanks are commonly in single clusters, and the boundaries between clusters and the magmatic segments are commonly mismatched (Extended Fig. A4). In Afar, the length scale of clusters is longer than the magmatic segments. We therefore interpret that the compositional variability is not related to the along axis segmentation of crustal sub-volcanic plumbing systems.



Instead we appeal to a deeper process. The data could be explained through a pulsing plume model (e.g., 9), as shown by the spline model and K-means cluster analysis. Rifts can act as natural channels that can be exploited by melt from mantle plumes [37]. Considering the extension rate in Afar (10.5–19.5 mm/yr; 18) compared to that of the MER (\sim 5.2 mm/yr; 18), it is plausible that a faster mantle flow rate, due to a channelling effect, occurs underneath Afar (38; 37). This may in turn result in a different length scale of melt characteristic variation (Figs. 3 & Extended Fig. A2) between the rifts (Extended Fig. A4). Further, a contrast in crustal thickness (and therefore inferred lithosphere thicknesses) is evident between the rifts, with the MER crust being thicker (25–33 km) compared to that of Afar (16 – 25 km; Extended Fig. A1f). This effect could also introduce a difference in mantle flow rate. A progressive thickening of the overlying lithosphere away from the plume centre in the MER reduces the volume capacity for melt, impeding the mantle flow. Consequently, the heterogeneous nature of the pulsating plume would likely exhibit a more condensed pattern within the MER compared to Afar (Extended Fig. A4).

We conclude that variations in melt composition and abundance within Afar is best explained by a heterogeneous pulsing mantle plume that is not symmetrical, but instead shaped by the varying extension rates within each rift. Although this model principally investigates the likelihood of a singular or three-plumelet scenario, our results demonstrate, that for either option, a heterogeneous plume provides the best match to observations in the region. The observed disparities in melt composition and abundance between the MER and Afar imply that segmentation within plume-assisted rift environments may be controlled not only by the plume itself but also by factors such as the extension rate of the rift and/or the crustal thickness. If this model is correct, therefore, it carries fundamental implications for understanding the dynamical evolution of magmatism within rifted margins.

5 Methods

Sample selection and processing

Samples and previously published data selected within this study must have been erupted from a volcano that has been active within the Holocene [17] with the age of the sample estimated to be of Quaternary age (i.e., $<$ 2.5 Ma). Samples had to be fresh, and their exact coordinates had to be known.

Obtaining previously published data

Previously published geochemical data was obtained from GEOROC, file name “*East African Rift part 1 & 2*” on 20th June 2022 (20). Once downloaded the data-files were then filtered to only include data within Ethiopia (including the Main Ethiopian Rift and Afar). Following this the data were further filtered using the following criteria:

1. The values for the sample must be that of the whole rock geochemistry, no mineral separates.
2. The individual sample must have major element, trace element, $^{87}\text{Sr}/^{86}\text{Sr}$, $^{143}\text{Nd}/^{144}\text{Nd}$, $^{206}\text{Pb}/^{204}\text{Pb}$, $^{207}\text{Pb}/^{204}\text{Pb}$ and $^{208}\text{Pb}/^{204}\text{Pb}$ isotope values.

3. The coordinates must be specific to the individual sample's location rather than an average coordinate for the area.

5.1 Analytical Geochemistry

Sampling and sample preparation

Ninety three lavas, eleven welded tuffs and one pumice sample, from various volcanoes in Afar (Ert A Ale Volcanic Segment, Ayelu, Abida, Yangudi, Dama Ali, Kerubm Ela, Didoli, Abbahu, Afdera, Tat Ali and Manda Hararo) were selected for geochemical analysis. The samples were collected during the CNR/CNRS projects in Afar during the 1960s [39] and stored in the Afar Repository at the University of Pisa, Italy, (<http://repositories.dst.unipi.it/index.php/home-afar>). A further 52 samples from the Boset-Bericha Volcanic Complex (BBVC) were collected during three field seasons, November 2012, April-May 2015 and February 2017 [40].

Sample preparation for major, trace and isotope analyses was carried out at the University of Southampton. Samples were cut with a saw to remove any heavily weathered sections, and any cut surfaces ground down to reduce any potential metal contamination from the saw blade. Rock samples were then crushed using a fly press, placed in double-layered plastic bags prior to crushing to minimise metal contamination.

The crushed material was separated into three size fractions (>1 mm, 0.5 mm to 1 mm, <0.5 mm) using Teflon sieves keeping the middle fraction (0.5 - 1 mm). The selected fraction was cleaned by ultrasonication in Milli-Q water then dried overnight in an oven at 85 °C. The cleaned rock chips were then hand-picked under a microscope, to remove any non-rock material and weathered grains. An aliquot of cleaned chips were used for Pb isotope analysis. For major element, trace element, and $^{143}\text{Nd}/^{144}\text{Nd}$ and $^{87}\text{Sr}/^{86}\text{Sr}$ isotope analysis, the remaining rock chips were ground to a fine powder using an agate mortar and pestle, to minimise metal contamination.

Trace element analysis

Samples were prepared for whole-rock trace element analysis using 0.05 g (for BBVC samples) or 0.075 g (for all other samples) powdered sample. The powdered samples were digested in sealed Savillex Teflon vials with 15 drops concentrated HNO_3 and 2 ml HF on a hotplate at 130 °C for 24 hours (for all other samples), or with 50 drops HF and 2 ml HNO_3 on a hotplate at 130 °C for 24 hours (for BBVC samples). The HNO_3/HF was evaporated off, and the samples were refluxed in 6M HCl for another 24 hours on a hotplate at 130 °C. The 6M HCl was evaporated off, and the samples were redissolved in 6M HCl. Mother solutions were prepared by adding 6M HCl and Milli-Q water (total 30 ml) to the dissolved samples. Daughter solutions were prepared using 0.5 ml of mother solution, diluted to 5 ml with 3% HNO_3 (containing the internal standards In/Re/Be), resulting in an overall dilution factor of c. 4000.

Trace element analyses of the daughter samples were undertaken on the ThermoScientific XSeries2 quadrupole inductively coupled plasma mass spectrometer (ICP-MS) at the University of Southampton. Analytical standards and accuracy were monitored

using international standards CBlk, JB-2, JB-3, BHVO2, AGV-2, BCR-2, BIR-1, JG-2 and JR-2, and internal standards BRR-1 and BAS206 (see Supplementary Data). Results in counts per second were processed with the exact calculated dissolution factors (see Supplementary Data) and blank corrections to produce concentrations in ppm for the trace elements analysed.

Pb isotopic analysis

For Pb isotope analysis, 0.3 g of cleaned, picked rock chips (0.5 mm to 1 mm) were weighted into dedicated Pb Savillex Teflon vials and leached on a hotplate with 4 ml 6M HCl for an hour (15 minutes for obsidian and pumice samples). Samples were rinsed several times in Milli-Q water, then 0.5 ml concentrated HNO₃ and 3-4 ml of concentrated HF were added. Samples were refluxed on a hotplate at 140 °C for 24 hours, and then evaporated to dryness. 0.5 ml concentrated HCl was added, and the sample evaporated to dryness, then 0.5 ml concentrated HNO₃ was added and again evaporated to dryness. The final residue was reconstituted in 0.5 ml HBr and refluxed for an hour. The samples were cooled and centrifuged for 5 minutes. Pb was isolated using a single-stage HCl anion-exchange chromatographic resin separation method [41], with AGX-1x8, 200 – 400 mesh resin. Following this, the Pb isolate was dried down, redissolved in HNO₃ and analysed using the double spike method of [42]. The samples were subsequently analysed on a ThermoScientific Neptune MC-ICPMS at the University of Southampton (UK) with a NBS SRM 981 reproducibility of ²⁰⁶Pb/²⁰⁴Pb = 16.9404 ± 32, ²⁰⁷Pb/²⁰⁴Pb = 15.4969 ± 32, ²⁰⁸Pb/²⁰⁴Pb = 36.7149 ± 90 (2sd; n=40).

¹⁴³Nd/¹⁴⁴Nd and ⁸⁷Sr/⁸⁶Sr isotopic analysis

For Sr and Nd analysis, remaining mother solutions from the preparation of trace element solutions (see method above) was used for all samples except BBVC. An aliquot of each mother solution was used, to give a volume of liquid containing at least 1 µg Sr and 200 ng Nd, and evaporated to dryness in Savillex Teflon vials on a hotplate at 130 °C. Sample residues were reconstituted in 200 µl 1.75M HCl.

For samples from the BBVC, rock chips to a weight containing at least 1 µg Sr and 250 ng Nd were used (250 mg for trachyte/rhyolite samples, 60 mg for intermediate/-mafic samples). Rock chips were leached in 4 ml 6M HCl for 30 minutes in Savillex Teflon vials (obsidian samples for only 15 minutes, to avoid dissolution of the sample). The samples were then rinsed with Milli-Q water and HNO₃, and then the same digestion procedure as for trace element analysis (above) was followed. The final mother solutions were made up using HCl and Milli-Q water to 30 ml for felsic samples and 20 ml for mafic samples.

All samples were then passed through ion exchange column chemistry, using a AG50-X8 200-400 mesh resin cation column to separate the Sr and Nd fractions. The sample fractions were then subsequently evaporated to dryness ready for further column chemistry.

Sr was further isolated through Sr-spec resin column, following the methodology of [43]. Samples were then evaporated to dryness, dissolved in 1.5 ml 1M HCl and loaded onto outgassed tantalum filaments with 1 µl of Ta-activator. Sr isotopic analysis was done on a ThermoScientific Triton Plus (TIMS) at the University of Southampton.

SRM NIST987 was used to monitor accuracy and gave average $^{87}\text{Sr}/^{86}\text{Sr}$ values of 0.710243 and samples are quoted relative to 0.710248, while reproducibility was ± 0.000020 (2sd; n=464).

The Nd aliquot from the cation column was followed by an Ln-spec resin (50-100 μm) [44]. The samples were then evaporated to dryness and 3% HNO_3 was added to produce a solution of 50 ppb. $^{143}\text{Nd}/^{144}\text{Nd}$ analyses were undertaken on the ThermoScientific Neptune multi-collector inductively coupled plasma mass spectrometer (MC-ICP-MS) at the University of Southampton. SRM JNdi-1 was used to monitor accuracy and produced an average $^{143}\text{Nd}/^{144}\text{Nd}$ of 0.512115 with an external reproducibility of ± 0.000006 (2sd) across 6 analysis sessions over 2 years. The total column blanks (i.e., when blank acid is run through the column procedure) were negligible (<20 pg) compared to the total amounts analysed (1 μg and 200 μg) for Sr and Nd respectively.

Ambient noise Rayleigh-wave phase velocity

For the velocity maps data from 13 temporary seismic networks and 5 permanent stations present from 1999 – 2017 from 3-component broadband seismometers were used. Seismograms were downsampled to 1Hz, normalized, and whitened with a 4th order Butterworth bandpass filter. 24-hour long waveforms were cross-correlated for each concurrent running station pair between the vertical components (C_{zz}) [45]. Cross-correlograms were stacked for every 24-hour period and for each station pair to improve the signal to noise ratio (SNR). Station pairs with interstation distances less than $3 \times$ wavelength (λ), SNR less than 3, or less than 10 days' worth of continuous recording were removed. This resulted in 34991 total cross-correlation functions and 6716 Noise Correlation Functions (NCF) for Rayleigh-waves [28; 21]. The fundamental mode Rayleigh-wave data were windowed using a time variable filter [46], and the Fourier amplitude and phase calculated at each frequency of interest via a fast Fourier transform.

Phase velocity dispersion curves were estimated using a spatial domain technique over the entire array. A zero order Bessel function of the first kind was fitted to the real part of the NCF in the Fourier domain by searching over phase velocities from 2.5–5 km/s in 0.01 km/s steps for every period of interest. For each stacked NCF the phase was measured at each period by unwrapping the phase using the average phase velocity curve at the longest periods, to resolve cycle ambiguity [47].

The Born approximation 2-D phase sensitivity kernels [48] and an iterative damped least squares approach [49; 50] were used to calculate 2-D phase velocity maps by using the equation:

$$\Delta m_i = (G^T C_{nn}^{-1} G + C_{mm})^{-1} (G^T C_{nn}^{-1} \Delta d + C_{mm}^{-1} [m_i - m_0]) \quad (1)$$

where m_i is the current model at iteration i , Δm_i is the change to the model after the next iteration, G is the matrix of partial derivatives from the kernel at each node [51], C_{nn} is the data covariance matrix, C_{mm} is the model covariance matrix, Δd is the difference between the observed and predicted phase, and m_0 is the starting model. The final term ($C_{mm}^{-1} [m_i - m_0]$) damps the model towards the initial model using the apriori model covariance.

A regular grid of nodes spaced $0.25^\circ \times 0.25^\circ$ was used and averaged the sensitivity kernel between each station pair onto the nodes (52; 53). The sensitivity kernel was calculated on a densely sampled grid ($0.1^\circ \times 0.1^\circ$) and then the Gaussian distance-weighted average taken to determine the value at each node on the coarser grid with a Gaussian smoothing width (2σ) of 40 km. The inversion estimates the average phase velocity at each node before we reverse the Gaussian weighted average to recover a $0.1^\circ \times 0.1^\circ$ sampled grid by determining the Gaussian weighted contribution of the nearest nodes to each pixel using the same 40 km Gaussian width which further smooths the kernels.

Teleseismic Rayleigh-wave phase velocity

Amplitude and phase information were extracted from vertical component seismograms for earthquakes with magnitude >5.5 and epicentral distances of $25 - 150^\circ$ resulting in 1053 teleseismic events that met our criteria [21]. The raw data were de-meanned, de-trended and their instrument response was removed. The data were bandpass filtered using a 4th order Butterworth filter with corner frequencies between $0.005 - 0.4$ Hz. The fundamental mode Rayleigh-wave data were windowed using a time variable filter [46], and the Fourier amplitude and phase calculated at each frequency of interest via a fast Fourier transform. To ensure robustness, the data were manually inspected for continuous dispersion curves, a $\text{SNR} > 3$ and peak energy between the approximate frequencies of interest, 0.01 to 0.07 Hz resulting in 1053 events and 47227 ray paths for the final inversion.

The average dispersion curve was determined for the area using a 1-D version of the two-plane wave inversion method [54] which was completed in two steps: The first stage utilised a simulated annealing method to fit the two plane wave parameters for each event, while trying a range of starting phase velocities for the model between $3.00 - 4.40$ km/s [55] which ensured a global starting model was found for input to the next stage. The second stage utilised an iterative damped least squares inversion [50] which simultaneously solved for the phase-velocity, azimuthal-anisotropy and wave parameters for each event. An apriori error of 0.2 km/s where assumed for the phase-velocity model parameters (square root of the diagonals of C_{mm}). The apriori error of the data (square root of the diagonals of C_{nn} , the data covariance matrix, Eq. 1) are initially assigned an arbitrary value of 0.2, and because the data is normalized to a maximum value of 1 for each event, this yielded a relatively conservative 20% error for the data. The apriori error in the data for each event after the initial inversion is defined by the misfit between the event data and the starting model of the previous iteration [54]. A minimum threshold for the apriori data covariance matrix of $(0.03)^2$ or roughly 3% error of our normalized data was set which are determined from the fits to the data as the inversion evolves. In other words 97% of the data is fitted to the normalized value of 1. The average event misfit was assigned to the individual teleseismic data apriori error for a given teleseismic event and was updated at each step during the inversion. The reweighting of the data has an effect similar to using an L1-norm, by minimizing the effect of outliers or poorly fit data.

2-D Phase-velocity maps were inverted for using the two plane wave method of [54] at each period using the amplitude and phase measurements described above from the teleseismic events, using 2-D finite frequency kernels (53; 48). The same

nodal parameterisation was used as in the ambient noise tomography, i.e., a $0.25^\circ \times 0.25^\circ$ nodal grid with the outermost row and column spaced at 1° to absorb velocity heterogeneities outside the target region. The average 1-D phase velocity described in the previous section is used as the starting model at each period. The inversion used 2-D finite frequency kernels (54; 56; 57; 53) and an iterative damped least squares approach (Eq. 1; 50), which solves for phase-velocity at each node, and the plane wave parameters for each teleseismic event. The same Gaussian averaging scheme described above was used to generate higher resolution phase velocity grids at $0.1 \times 0.1^\circ$. The phase velocity at the nodes represent an average phase over the smoothed area around the node, so the final phase velocity maps at $0.1 \times 0.1^\circ$ resolution are determined from the Gaussian distance weighted contributions of the nearest nodes to each pixel. An apriori model covariance of $(0.2 \text{ km/s})^2$ was used for the inner nodes and $(2 \text{ km/s})^2$ for the outer nodes which was used to absorb velocity heterogeneity outside the array along the diagonals of C_{mm} . The inversion was run twice and events with phase misfits of >4 s were removed from the starting dataset after the first iteration and used as the input for the final set of inversions. The removal of these poorly fit events is necessary as it removes waveforms with complicated source radiation patterns and other effects not accounted for in the inversion.

Shear velocity maps from joint inversion of teleseismic and ambient noise Rayleigh-wave phase velocities

The shear velocity maps were produced by inverting each pixel of the phase velocity maps for a 1-D shear-velocity model at every pixel as a function of depth. The combined 1-D shear velocities at each pixel, form the 3-D volume. Phase velocity maps from 8 – 26 s were used from the ambient noise dataset and from 29 – 100 s from the teleseismic dataset. The transition at 26 s from one data-type to another was chosen based on the relative amounts of data, i.e., where the teleseismic had a greater number of ray paths. Where the ambient noise and teleseismic phase velocity maps overlap, they are within uncertainty of one another [21].

An iterative damped least squares inversion was used [50] and the shear velocity parameterised every 5 km vertically with $0.1^\circ \times 0.1^\circ$ pixel size for the upper 50 km. For deeper depths an irregular spacing was used increasing from 10 – 50 km spacings to match that of [30]. The partial derivatives that relate variations in shear velocity to changes in phase velocity were calculated using DISPER80 [51] and assigned a nominal apriori standard error for each model parameter of 0.2 km/s for shear velocity. V^p/V^s was fixed to 1.80, the crustal average from receiver function analyses (e.g., 58) and also a typical mantle value [59]. Variations in V^p/V^s (1.5–2.1, the observed V^p/V^s ratios in this area), and scaling parameters, produced results within uncertainty.

The shear velocity model was interpolated to 1 km depth using a linear interpolation and we extracted 1D columns of velocity with depth at the same resolution as our pixel size.

Moho depths

The gridded Moho depth map was produced from the V^s maps of [28] described above. The V^s model was interpolated to a vertical grid spacing of 1 km and a velocity slice at the 3.75 km/s contour was extracted which mapped best to previous receiver

function measurements (60; 61; 58; 62; 63), active source experiments (e.g., 64) and previous S-wave models (e.g., 65).

GIS Interpolation We use an in-built spline interpolation function within ArcGIS Pro 3.0.2 to investigate the regional spatial patterns for each variable. The spline model has two conditions: (1) The surface must pass through each data point exactly, and (2) The curvature of the surface must be minimised, which involves minimising the sum of squares of its gradient. We apply a regularized spline model with a weight of the third derivative (τ) set to zero, and use 12 points to calculate each interpolated cell. The algorithm for the spline interpolation is:

$$S(x, y) = T(x, y) + \sum_{j=1}^N \lambda_j R(r_j) \quad (2)$$

where $j = 1:N$, N is the number of points (i.e., 12), λ_j are the coefficients for the system (solved by linear equations), r_j is the distance from point (x, y) to the j th point,

$$T(x, y) = a_1 + a_2x + a_3y \quad (3)$$

where a_i are coefficients for the system (solved by linear equations) and

$$R(r) = \frac{1}{2\pi} \left(\frac{r^2}{4} \left[\ln\left(\frac{r}{2\tau}\right) + c - 1 \right] + \tau^2 \left[K_o\left(\frac{r}{\tau}\right) + c + \ln\left(\frac{r}{2\pi}\right) \right] \right) \quad (4)$$

where r is the distance between the point and sample, τ^2 is the weight parameter, K_o is the modified Bessel function and c is a constant equal to 0.577215.

5.2 Statistical Analyses

Models considered

Five models were considered (see Table 1), with each model being tested using a linear fit and a spline fit. It should be noted that a spline fit can fit a linear pattern to the data if that is the best-fitting line.

Empirical models are estimated for the variation of each of 14 geochemical quantities (each of which is represented generically by random variable Y) as a function of distance $d \in [0, 1800]$ km for five different models. Models are specified which explore the variation of Y with d in increasing complexity. The simplest model (C1C) assumes the existence of a single plume centre (at 11.192 °N 41.784 °E), with respect to which d is defined for all three rifts; the variation of Y with d is assumed common to all rifts. Model C3C assumes the existence of three plume centres (at 11.192 °N 41.784 °E, 14.008 °N 40.458 °E & 6.626 °N 37.948 °E); observations are allocated to the nearest plume centre, facilitating calculation of a single d for each observation; the variation of Y with d is assumed common to all rifts, regardless of plume allocation. Model C1D assumes one plume centre (like C1C) for calculation of d , but now the variation of Y

Model	Description
C1C	A singular plume centred at Lake Abhe (11.192°N 41.784°E) with each rift (i.e., Red Sea Rift, Gulf of Aden rift and Main Ethiopian Rift) behaving the same (not independent), based on the theory of [5]. This model fits a single line using all the data points from each rift.
C3C	Three plumes centred at Lake Abhe (11.192°N 41.784°E), and two other points across the region (14.008°N 40.458°E & 6.626°N 37.948°E); a model based on the locations of previously proposed plumelet locations through numerical modelling [29]. Assumes each rift behaves the same (not independent of each other) and the plumes are of the same composition. This model fits a single line across all the data points. 
C1D	A singular plume centred at Lake Abhe (11.192°N 41.784°E) with each rift behaving independently. This model fits three lines (one for each rift) across the data points for the corresponding rift.
C3D	Three plumes centred at Lake Abhe (11.192°N 41.784°E), and two other points across the region (14.008°N 40.458°E & 6.626°N 37.948°E) with each rift acting independently. This model assumes each plume is compositionally the same and fits three lines (one for each rift) across the data points for the corresponding rift.
C3X	Three plumes centred at Lake Abhe (11.192°N 41.784°E), and two other points across the region (14.008°N 40.458°E & 6.626°N 37.948°E) with each rift and plume acting independently. This model plots five lines.

Table 1 Models considered when assessing the Afar plume characteristics. Details of each model are described.

with d is assumed to be different across rifts. Model C3D copies C3C for estimation of d , but variation of Y with d is assumed to be different across rifts. Finally, in model C3X we consider the presence of three plume centres, with different variation of Y with d for each combination of plume and rift.

Data pre-processing

For models C1C and C1D the distance between each sample and the plume centred on Lake Abhe ($11.192170^{\circ}\text{N}$ $41.783750^{\circ}\text{E}$) is calculated. For models C3C, C3D and C3X, the distance between each sample and each of the three plume locations is calculated, and then each sample is assigned to its nearest plume centre. The distance (d) between two locations (i.e., plume and sample) is calculated using the spherical cosine law:

$$d = R(\cos^{-1}(\cos(a)\cos(b) + \sin(a)\sin(b)\cos(C))) \quad (5)$$

where a is the angle (in radians) from the North Pole to the sample location, b is the angle (in radians) from the North Pole to the plume location, C is the difference in radians between the longitude values of the sample and plume, and R is the radius of the earth in metres (6371×10^3). 

Penalised B-splines

For each model, the variation of Y with d (possibly for a subset of the full sample) is described using a penalised B-spline (e.g., 66; 67), the characteristics of which are selected to provide optimal predictive performance. First, for a large index set of locations equally spaced on the domain of distance, we calculate a B-spline basis matrix B (e.g., 68) consisting of p ~~equally-spaced~~-cubic spline basis functions. Then the value of Y on the index set is given by the vector $B\beta$, for spline coefficient vector β to be estimated. The value of p is specified to be sufficiently large to provide a good description of a highly variable Y . For a given data set, we penalise the difference between consecutive values in β using a roughness penalty, such that the penalised spline provides optimal predictive performance.

Estimating optimal spline roughness and predictive performance

For a sample of n_1 training data, consisting of vectors of geochemical quantities (y_1) and distances (d_1), we first allocate each element of d_1 to its nearest neighbour in the index set, and hence construct the appropriate spline basis matrix B_1 for the sample. We then assume that $y_1 = B_1\beta + \epsilon$, where the elements of ϵ are independently and identically-distributed zero-mean Gaussian random variables. We penalise the roughness of β using a first-different penalty $\lambda\beta'P\beta$, where $P=D'D$ and D is a first difference matrix (with elements $D_{ij} = -1$ if $i = j$; $= 1$ if $j = i+1$; and $= 0$ otherwise; e.g., [69]). For a given choice of λ , we then find the optimal value of β by minimising lack of fit

$$\beta^*(\lambda) = \operatorname{argmin}_{\beta} (y_1 - B_1\beta)'(y_1 - B_1\beta) + \lambda\beta'P\beta \quad (6)$$

$$= (B_1'B_1 + \lambda P)^{-1}B_1'y_1. \quad (7)$$

We can evaluate the predictive performance of the resulting spline description using a tuning set of n_2 observations (independent of the training set) represented by vectors y_2 and d_2 . We again start by finding the appropriate spline basis matrix B_2 for this sample. Then we can calculate the predictive mean square error for the tuning sample

$$\text{MSE}_2(\lambda) = \frac{1}{n_2}(y_2 - B_2\beta^*(\lambda))'(y_2 - B_2\beta^*(\lambda)) \quad (8)$$

for each of a set of representative choices of values for λ . We can then select the optimal value of λ using

$$\lambda^* = \operatorname{argmin}_{\lambda} \text{MSE}_2(\lambda). \quad (9)$$

The value $\text{MSE}_2(\lambda^*)$ is a biased estimate of predictive performance, since the value of λ^* was tuned to minimise its value. We can obtain an unbiased estimate for the predictive performance of the spline model using a test set of n_3 observations (independent of the training and tuning sets) represented by vectors y_3 and d_3 (and corresponding spline basis matrix B_3). Then the predictive performance is estimated

using

$$\text{MSE} = \frac{1}{n_3} (y_3 - B_3 \beta^*(\lambda^*))' (y_3 - B_3 \beta^*(\lambda^*)). \quad (10)$$

Cross-validation and model comparison

We exploit cross-validation to evaluate MSE, by partitioning the full sample of data into $k > 2$ groups at random, withholding one group for tuning, another group for testing, retaining the remaining $k - 2$ groups for training. We then loop exhaustively over all possible combinations of choice of train, tune and test groups, evaluating overall predictive performance on the test data over all iterations, noting that each observation occurs exactly once in the test set. For models (C1D, C3D, C3X) requiring separate model fits to subsets of data, MSE is estimated using predictions from optimal predictive models for each subset. Further, we can repeat the analysis for different initial random partitioning of observations into k groups, to assess the sensitivity of overall predictive performance to this choice. We are careful to use the same cross-validation partitions to evaluate each of the five models, so that predictive performances can be compared fairly.

To quantify model performance over all 14 geochemical quantities, we define the overall standardised MSE



$$\text{SMSE} = \sum_{j=1}^{14} \frac{\text{MSE}_j}{s_j^2} \quad (11)$$

where MSE_j is the predictive performance for the j^{th} quantity, and s_j^2 is the sample estimate for the variance of that quantity.

Linear regression



For comparison, we also evaluate linear regression models for the variation of Y with d . In the current notation, these can be thought of as simple models with basis matrix $B = [\mathbf{1} \ d]$, where $\mathbf{1}$ is a vector of appropriate length with each element = 1. β in this case is a 2-vector with elements corresponding to intercept and slope coefficients. Linear regression is approached using penalised B-spline models as the roughness coefficient $\lambda \rightarrow \infty$. That is, linear regression corresponds to a penalised B-spline model with very large λ . Therefore, a penalised B-spline model is guaranteed to perform at least as well as linear regression.

Principal Component Analysis



Principal component analysis (PCA) requires each sample or object to have the same number of values for each variable. Eleven variables ($^{206}\text{Pb}/^{204}\text{Pb}$, $^{207}\text{Pb}/^{204}\text{Pb}$, $^{208}\text{Pb}/^{204}\text{Pb}$, $^{143}\text{Nd}/^{144}\text{Nd}$, $^{87}\text{Sr}/^{86}\text{Sr}$, Ce/Pb , ΔNb , La/Sm , V_s at 40 km, V_s at 80 km, V_s at 120 km) were identified, that can be used to indicate the presence of a mantle plume, reducing the sample set to containing 95 samples. PCA is only carried out on radiogenic isotope compositions of the samples where data are available for the mantle end members (Afar plume, Pan-African lithosphere, and depleted mantle)

investigated. Each object is standardised before being included in the PCA:

$$y_{\text{std}j} = \frac{y_j - \bar{y}_j}{\sigma_j} \quad (12)$$

where \bar{y}_j is the mean of variable j , and σ_j is the standard deviation of the variable j :

$$\sigma_j = \sqrt{\frac{\sum (y_j - \bar{y}_j)^2}{N_j}} \quad (13)$$

where N_j is the number of objects within variable j .

Approximately 92% of the variance is explained within the plane of the first two eigenvectors, increasing to 96.7% when including the third eigenvector. The first principal component (PC-1) is most influenced by $^{207}\text{Pb}/^{204}\text{Pb}$, $^{208}\text{Pb}/^{204}\text{Pb}$, $^{143}\text{Nd}/^{144}\text{Nd}$ and $^{87}\text{Sr}/^{86}\text{Sr}$, whereas the second principal component (PC-2) is dominantly influenced by $^{206}\text{Pb}/^{204}\text{Pb}$ with minor influence from $^{208}\text{Pb}/^{204}\text{Pb}$ and $^{87}\text{Sr}/^{86}\text{Sr}$. The third principal component (PC-3) is dominated by $^{87}\text{Sr}/^{86}\text{Sr}$.

K-means cluster analysis

 K-means cluster analysis [70] is carried out on the samples using the eleven standardised variables, which are $^{206}\text{Pb}/^{204}\text{Pb}$, $^{207}\text{Pb}/^{204}\text{Pb}$, $^{208}\text{Pb}/^{204}\text{Pb}$, $^{143}\text{Nd}/^{144}\text{Nd}$, $^{87}\text{Sr}/^{86}\text{Sr}$, Ce/Pb, La/Sm, ΔNb , shear-wave speed at 40 km, shear-wave speed at 80 km, shear-wave speed at 120 km. The K-means algorithm assigns each object to a singular cluster that does not overlap with another (i.e., partitional clustering), minimising the total sum of squared error (SSE) from the centre point of each cluster, known as the centroid, to each object.

To find the optimum number of clusters (k), i.e., which reduces the within-cluster total sum of squares error with the lowest number of clusters, we run the K-means algorithm specifying k to be 1:20, over 1000 iterations for each k (Fig. A3). We then select eight clusters based on $k=8$ reducing the within-cluster total sum of squares by 75% from $k=1$, and the range over the 1000 iterations being minimised when $k \geq 8$. The cluster assignments for each object, out of the 1000 iterations, are selected by finding the iteration number that is closest to the mean within-cluster total sum of squares of that k value (shown by the blue line in Fig. A3).

Appendix A Supplementary Material

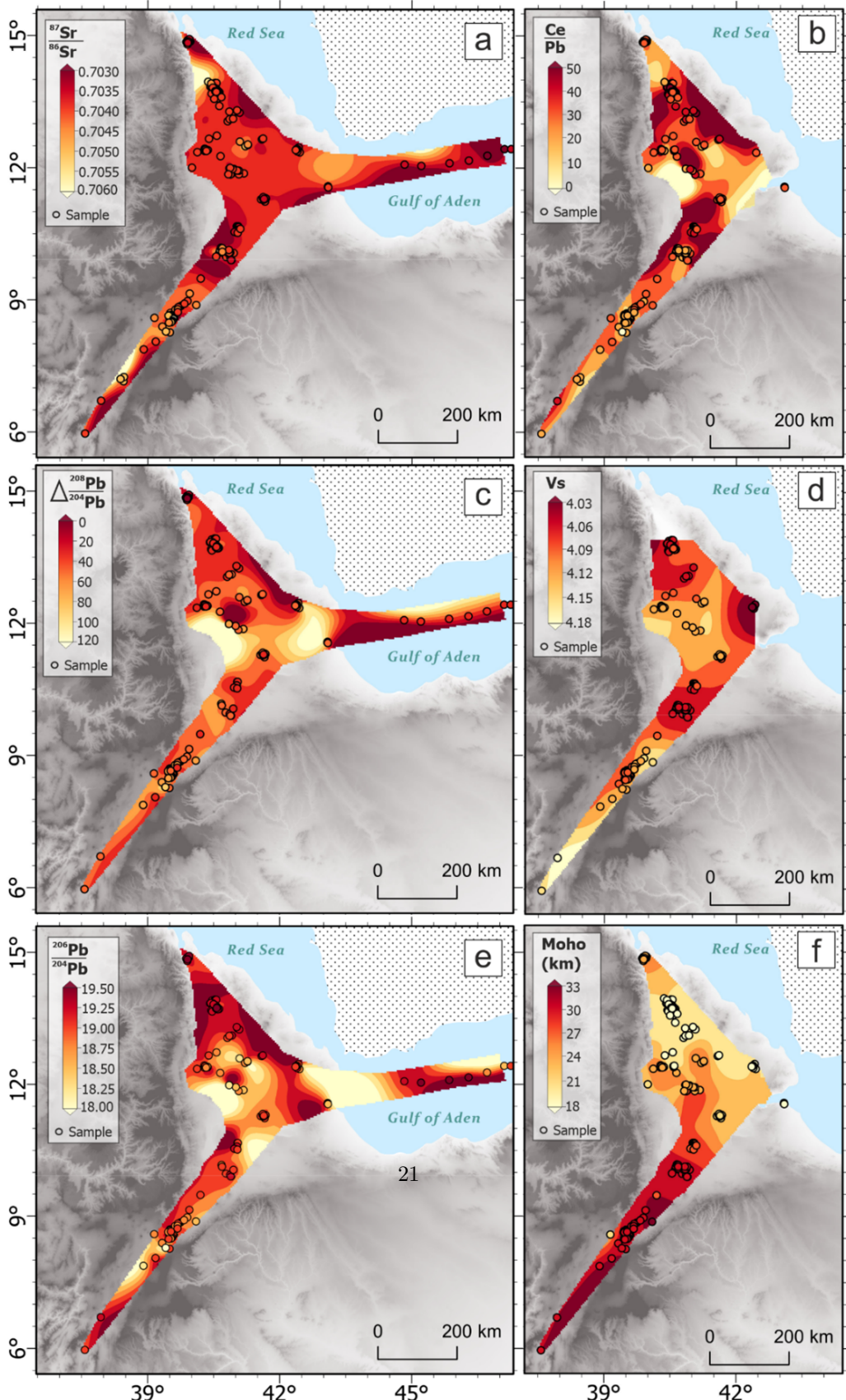


Fig. A1 Interpolated maps showing the patterns for the selected variables (see Section 5 for further details) across the study region. (a) $^{87}\text{Sr}/^{86}\text{Sr}$; (b) Ce/Pb; (c) $\Delta^{208}\text{Pb}/^{204}\text{Pb}$; (d) Shear wave velocity (V_s) at 120 km; (e) $^{206}\text{Pb}/^{204}\text{Pb}$; (f) Moho depth (km).

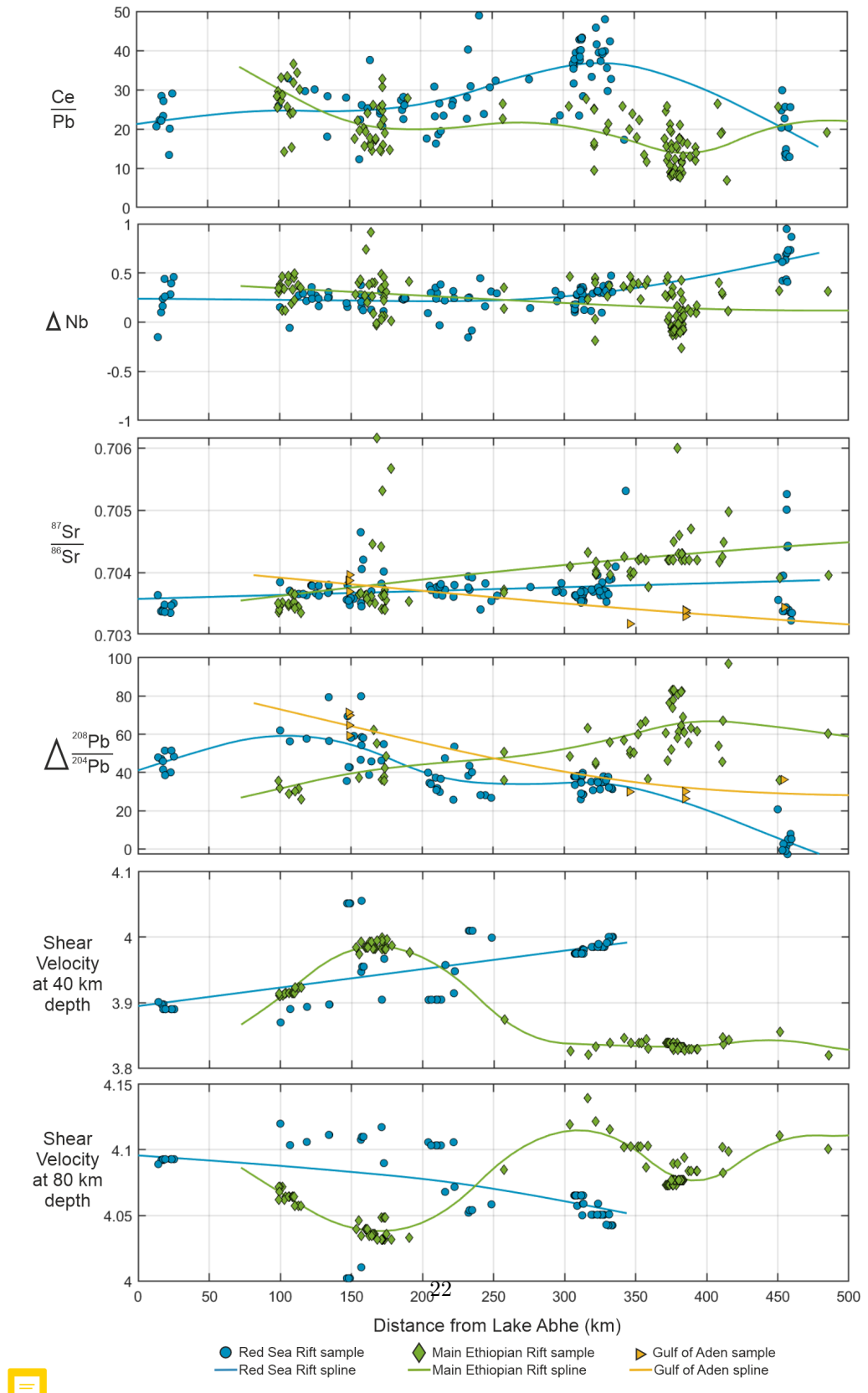


Fig. A2 Splines (lines) of the winning model (C1C) for remaining selected variables not shown in Figure 3. Symbols show the data within the study (blue circles = Red Sea Rift, green diamonds = Main Ethiopian Rift, yellow triangles = Gulf of Aden Rift).

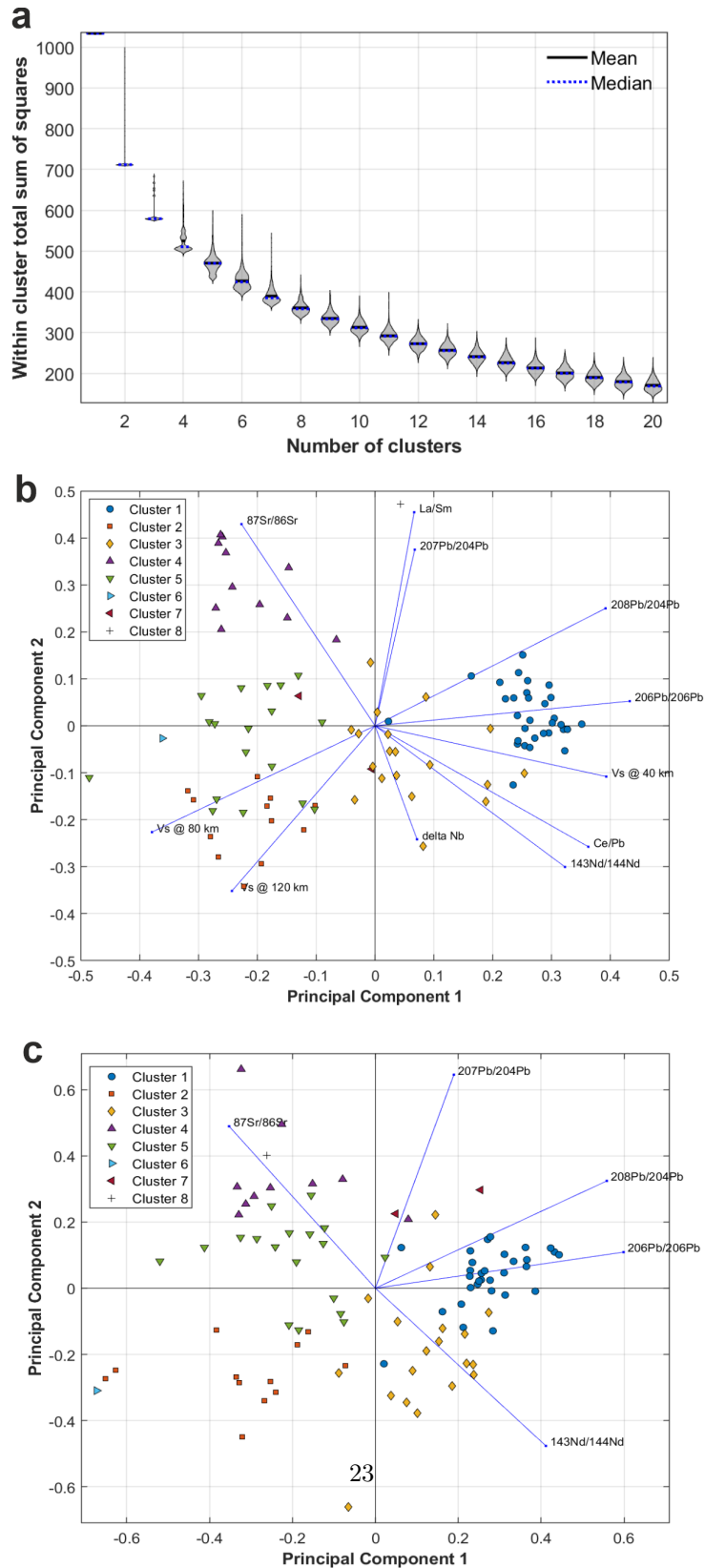


Fig. A3 (a) Violin plot showing the within cluster sum of squares for the k -means cluster analysis testing number of clusters between 1 and 20, for 1000 iterations. (b) Bi-plot of principal components 1 and 2 when considering all 11 variables. Symbology as in Figure A4. (c) Bi-plot of the principal components 1 and 2, when considering only the five isotopic variables. Symbology as in Figure A4.

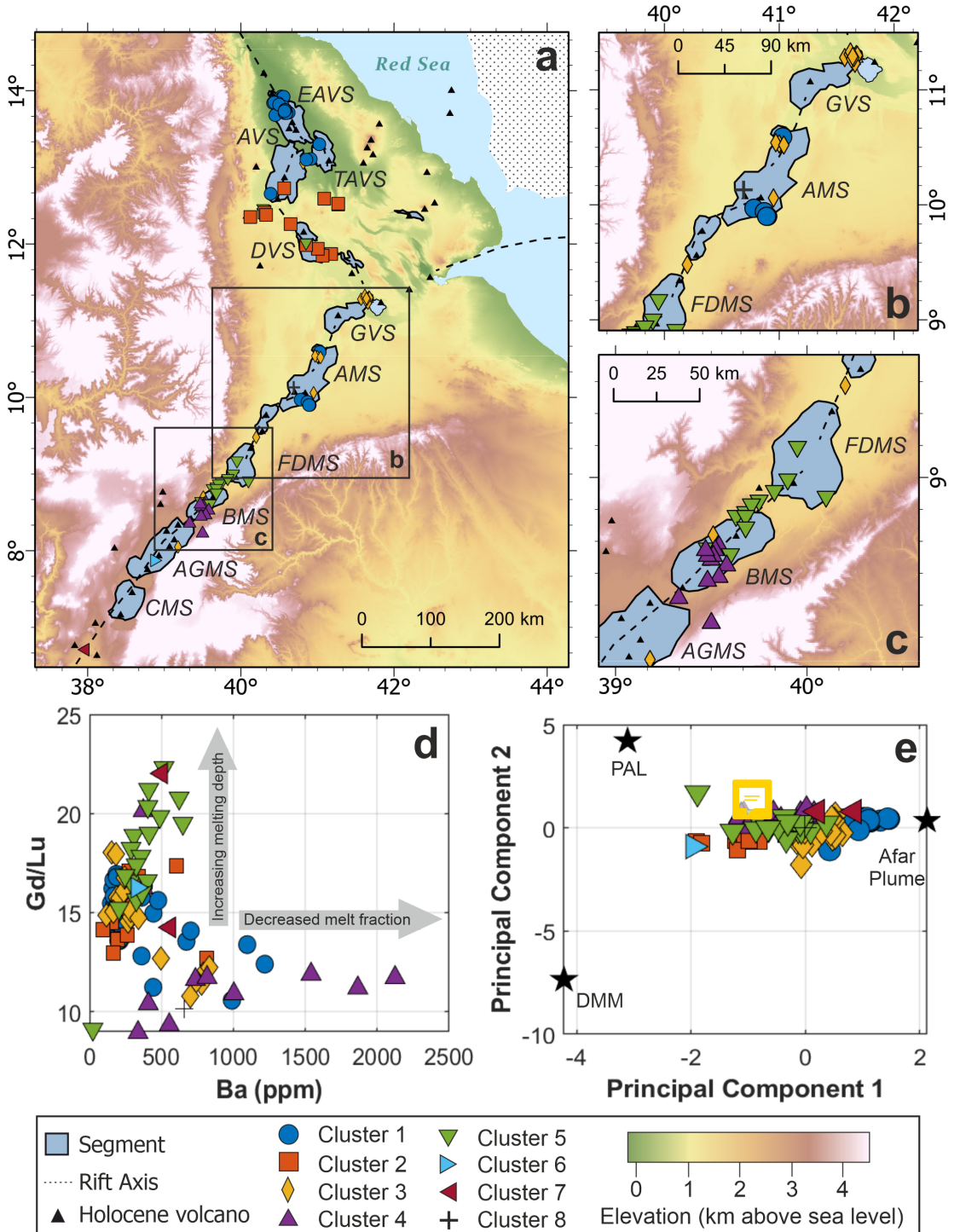


Fig. A4 Map of the segments and cluster assignment (see legend) within the study region. Segments are shown in blue from north to south: Erta Ale V₂₄anic Segment (EAVS), Tat'Ale Volcanic Segment (TAVS), Alayta Volcanic Segment (AVS), Dabbahu Volcanic Segment (DVS), Gabillema Volcanic Segment (GVS), Adda'do Magmatic Segment (AMS), Fentale-Dofen Magmatic Segment (FDMS), Boset Magmatic Segment (BMS), Aluto-Gedamsa Magmatic Segment (AGMS), Corbetti Magmatic Segment (CMS). Rift axis (dotted line) and Holocene volcanoes (black triangles) are shown. (b) and (c) are enlarged maps of the boxes shown in (a). (d) A plot of the Gd/Lu ratio (a proxy for melting depth) against the Barium (Ba) concentration in ppm (a tracer for melting extent) for the samples. (e) Principal component analysis bi-plot (PC1 vs PC2) when considering the five isotopic systems (see Section 5) showing the samples and their component scores relative to those of the mantle end-members.

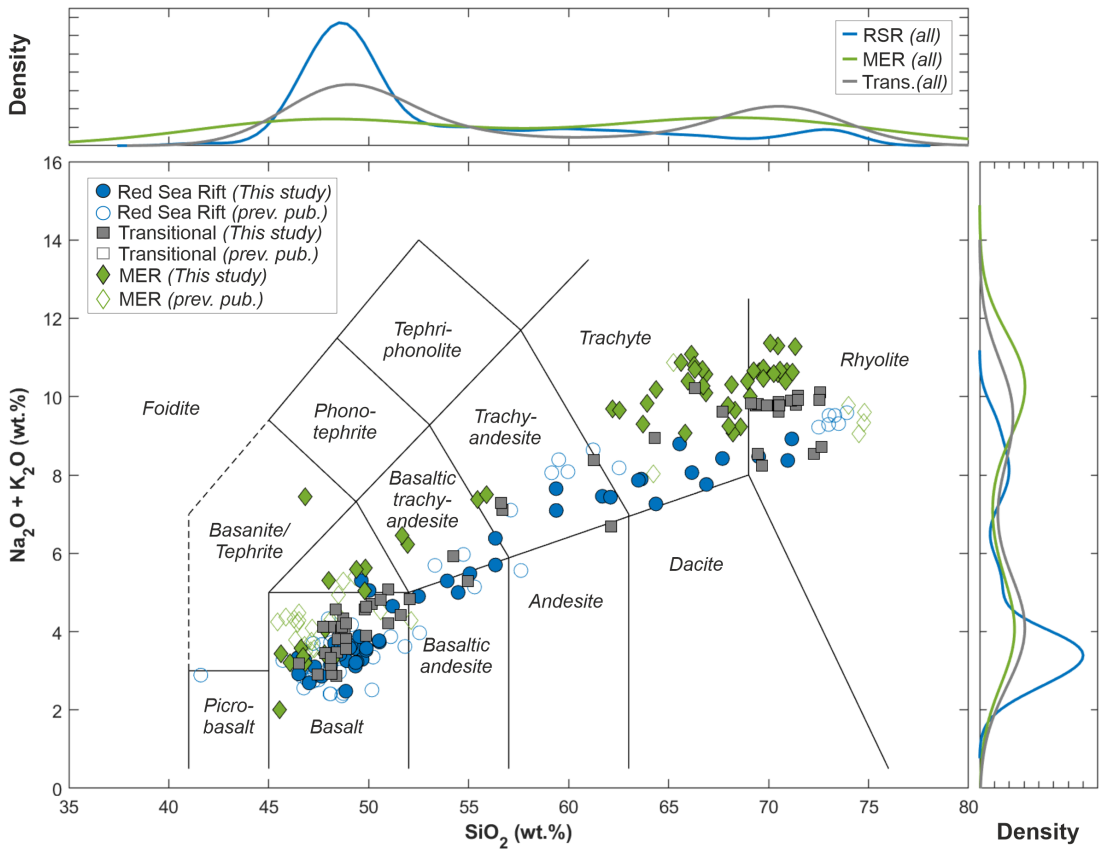


Fig. A5 Total alkali – silica (TAS) diagram showing the compositions for the data from our study (filled) and previously published data (hollow) for the Red Sea Rift (blue circles) and the Main Ethiopian Rift (MER; green diamonds). Samples that are debated to be on either rift are labelled transitional (grey squares).

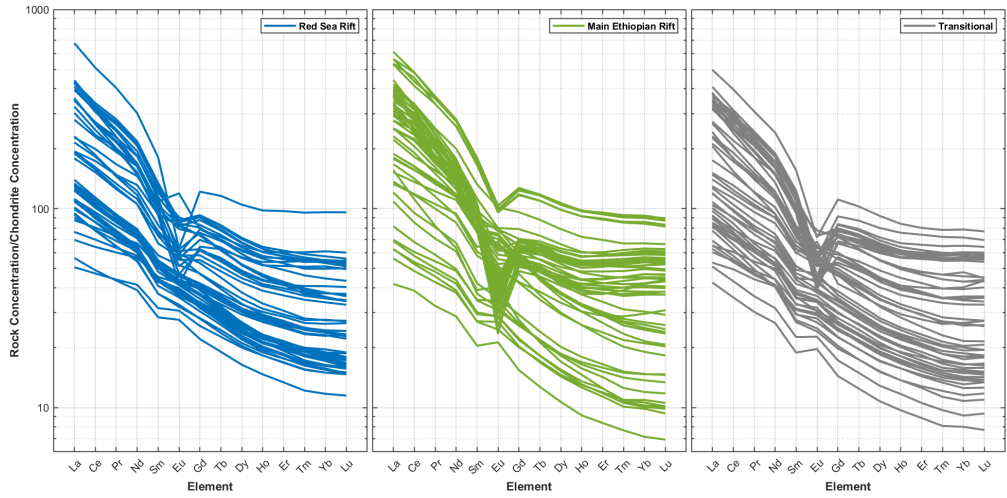


Fig. A6 Rare Earth Element plots showing the compositions observed at the Red Sea Rift (left, blue), MER (middle, green) and transitional (i.e., around the triple junction; right, grey). All compositions were normalised using chondrite values from [71].

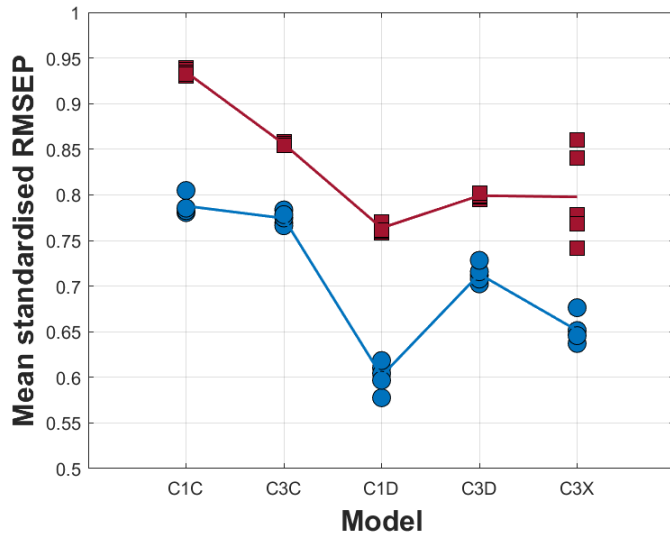


Fig. A7 The mean standardised root mean square error of prediction (RMSEP) for each of the models tested (described in Section 5.5) when excluding any observations that have a Ce/Pb > 20. Individual linear model results are shown by red squares and the mean of those results are displayed by the red line. Individual spline results are shown by blue circles and the mean of those results are shown by a blue line.

Table A1: Variables used within the analysis summarising the ranges observed and why they have been selected. References in the table are as follows: [72] [1]; [73] [2]; [15] [3]; [35] [4]; [23] [5]; [74] [6]; [34] [7]; [5] [8]; [24] [9]; [28] [10].

Variable	Observed Range	Details
$^{206}\text{Pb}/^{204}\text{Pb}$	17.853 to 19.608	$^{206}\text{Pb}/^{204}\text{Pb} > 20$ is linked to HIMU, $^{206}\text{Pb}/^{204}\text{Pb}$ ranging from 19.2 to 20.5 indicates a mantle plume source (C, FOZO) [1] and $^{206}\text{Pb}/^{204}\text{Pb} < 17.8$ can be related to a depleted mantle component [2]
$^{207}\text{Pb}/^{204}\text{Pb}$	15.448 to 15.697	$^{207}\text{Pb}/^{204}\text{Pb} < 15.5$ is related to a depleted mantle component [2], $^{207}\text{Pb}/^{204}\text{Pb} > 15.65$ is linked to the HiMU component and $^{207}\text{Pb}/^{204}\text{Pb} \sim 15.6$ indicates a mantle plume source (C, FOZO). A $^{207}\text{Pb}/^{204}\text{Pb} > 15.75$ is linked to crustal values [3, 4]
$^{208}\text{Pb}/^{204}\text{Pb}$	37.984 to 39.420	$^{208}\text{Pb}/^{204}\text{Pb} < 38$ is related to a depleted mantle component [2], $^{208}\text{Pb}/^{204}\text{Pb} > 39.5$ is linked to the HiMU component and $^{208}\text{Pb}/^{204}\text{Pb} 39.2$ to 39.5 indicates a mantle plume source (C, FOZO). A $^{208}\text{Pb}/^{204}\text{Pb} > 39.7$ is linked to crustal values [3, 4]
$^{143}\text{Nd}/^{144}\text{Nd}$	0.51259 to 0.51317	A low $^{143}\text{Nd}/^{144}\text{Nd} (< 0.5121)$ indicates continental crust or Pan African Lithosphere. $^{143}\text{Nd}/^{144}\text{Nd}$ values ~ 0.51285 indicates a HIMU or plume related mantle source. Higher $^{143}\text{Nd}/^{144}\text{Nd}$ values (> 0.5131) indicate a depleted mantle source (i.e., DMM) [1, 5, 6]
$^{87}\text{Sr}/^{86}\text{Sr}$	0.70280 to 0.70678	A low $^{87}\text{Sr}/^{86}\text{Sr}$ (0.7040-0.7045) indicates a mantle component that is either depleted (DMM) or a plume (HIMU, C). A higher $^{87}\text{Sr}/^{86}\text{Sr} (< 0.705)$ indicates the potential influence from continental crust [1, 5, 6]
Ce/Pb	6.84 to 48.92	A Ce/Pb > 30 is commonly attributed to a recycled mantle source that has been depleted in fluid mobile elements (i.e., Pb, Ba, Sr, K) during subduction, therefore resulting in high fluid-immobile-element to fluid-mobile -element ratios (i.e., Ce/Pb). Typical mantle has a Ce/Pb value of 25 ± 5 and crust a value of ~ 4 [7].

La/Sm	0.4 to 4.7	(La/Sm) >1 indicates LREE enrichment fractionation (alkali basalts or plume), (La/Sm) <1 indicates LREE depleted (mid-ocean ridge). The higher the La/Sm the lower the melt fraction [8]
ΔNb	-0.26 to 0.95	Differentiates between a depleted mantle ($\Delta\text{Nb} < 0$) and a mantle plume ($\Delta\text{Nb} > 0$) [9]
Vs @ 40 km	3.81 to 4.06	Shear wave velocities can be sensitive, temperature, grainsize and the presence of fluids. A reduction in Vs can indicate a change in mantle composition or an increased proportion of melt/hydrothermal fluid [10]. This is the velocity from 40 km depth.
Vs @ 80 km	4.00 to 4.16	Shear wave velocities can be sensitive, temperature, grainsize and the presence of fluids. A reduction in Vs can indicate a change in mantle composition or an increased proportion of melt/hydrothermal fluid [10]. This is the velocity from 80 km depth.
Vs @ 120 km	4.03 to 4.10	Shear wave velocities can be sensitive, temperature, grainsize and the presence of fluids. A reduction in Vs can indicate a change in mantle composition or an increased proportion of melt/hydrothermal fluid [10]. This is the velocity from 120 km depth.

References

- [1] Cañón-Tapia, E., Walker, G.P.L.: Global aspects of volcanism: the perspectives of “plate tectonics” and “volcanic systems”. *Earth-Science Reviews* **66**(1-2), 163–182 (2004) <https://doi.org/10.1016/j.earscirev.2003.11.001>
- [2] Morgan, W.J.: Convection Plumes in the Lower Mantle. *Nature* 1971 **230**:5288–230(5288), 42–43 (1971) <https://doi.org/10.1038/230042a0>
- [3] White, R., McKenzie, D.: Magmatism at rift zones: the generation of volcanic continental margins and flood basalts. *Journal of Geophysical Research* **94**(B6), 7685–7729 (1989) <https://doi.org/10.1029/JB094IB06P07685>
- [4] Rooney, T.O.: The Cenozoic magmatism of East Africa: Part IV – The terminal

- stages of rifting preserved in the Northern East African Rift System. *Lithos* **360-361** (2020) <https://doi.org/10.1016/j.lithos.2020.105381>
- [5] Schilling, J.-G.: Afar Mantle Plume: Rare Earth Evidence. *Nature Physical Science* **242**(114), 2–5 (1973) <https://doi.org/10.1038/physci242002a0>
 - [6] Rychert, C.A., Hammond, J.O.S., Harmon, N., Michael Kendall, J., Keir, D., Ebinger, C., Bastow, I.D., Ayele, A., Belachew, M., Stuart, G.: Volcanism in the Afar Rift sustained by decompression melting with minimal plume influence. *Nature Geoscience* **5**(6), 406–409 (2012) <https://doi.org/10.1038/ngeo1455>
 - [7] Ito, G.: Reykjanes 'V'-shaped ridges originating from a pulsing and dehydrating mantle plume. *Nature* 2001 **411**:6838 **411**(6838), 681–684 (2001) <https://doi.org/10.1038/35079561>
 - [8] Parkin, C.J., Lunnon, Z.C., White, R.S., Christie, P.A.F.: Imaging the pulsing Iceland mantle plume through the Eocene. *Geology* **35**(1), 93 (2007) <https://doi.org/10.1130/G23273A.1>
 - [9] Taylor, R.N., Davila-Harris, P., Branney, M.J., Ruth Farley, E.M., Gernon, T.M., Palmer, M.R.: Dynamics of a chemically pulsing mantle plume. *Earth and Planetary Science Letters* **537**, 116182 (2020) <https://doi.org/10.1016/j.epsl.2020.116182>
 - [10] Jackson, M.G., Becker, T.W., Steinberger, B.: Spatial Characteristics of Recycled and Primordial Reservoirs in the Deep Mantle. *Geochemistry, Geophysics, Geosystems* **22**(3) (2021) <https://doi.org/10.1029/2020GC009525>
 - [11] Rogers, N., Macdonald, R., Fitton, J.G., George, R., Smith, M., Barreiro, B.: Two mantle plumes beneath the East African rift system: Sr, Nd and Pb isotope evidence from Kenya Rift basalts. *Earth and Planetary Science Letters* (2000) [https://doi.org/10.1016/S0012-821X\(00\)00012-1](https://doi.org/10.1016/S0012-821X(00)00012-1)
 - [12] Zwaan, F., Corti, G., Keir, D., Sani, F.: A review of tectonic models for the rifted margin of Afar: Implications for continental break-up and passive margin formation. *Journal of African Earth Sciences* **164**, 103649 (2020) <https://doi.org/10.1016/j.jafrearsci.2019.103649>
 - [13] Ferguson, D.J., MacLennan, J., Bastow, I.D., Pyle, D.M., Jones, S.M., Keir, D., Blundy, J.D., Plank, T., Yirgu, G.: Melting during late-stage rifting in Afar is hot and deep. *Nature* **499**(7456), 70–73 (2013) <https://doi.org/10.1038/nature12292>
 - [14] Hansen, S.E., Nyblade, A.A.: The deep seismic structure of the Ethiopia/Afar hotspot and the African superplume. *Geophysical Journal International* **194**(1), 118–124 (2013) <https://doi.org/10.1093/gji/ggt116>
 - [15] Schilling, J.G., Kingsley, R.H., Hanan, B.B., McCully, B.L.: Nd-Sr-Pb isotopic

- variations along the Gulf of Aden: evidence for Afar mantle plume-continental lithosphere interaction. *Journal of Geophysical Research* **97**(B7) (1992) <https://doi.org/10.1029/92jb00415>
- [16] Hagos, M., Koeberl, C., Vries, B.: The Quaternary volcanic rocks of the northern Afar Depression (northern Ethiopia): Perspectives on petrology, geochemistry, and tectonics. *Journal of African Earth Sciences* **117**, 29–47 (2016) <https://doi.org/10.1016/J.JAFREARSCI.2015.11.022>
- [17] Smithsonian Institution: Global Volcanism Program (2013)
- [18] Zwaan, F., Corti, G., Sani, F., Keir, D., Muluneh, A.A., Illsley-Kemp, F., Papini, M.: Structural Analysis of the Western Afar Margin, East Africa: Evidence for Multiphase Rotational Rifting. *Tectonics* **39**(7) (2020) <https://doi.org/10.1029/2019TC006043>
- [19] Gillard, M., Leroy, S., Cannat, M., Sloan, H.: Margin-to-Margin Seafloor Spreading in the Eastern Gulf of Aden: A 16 Ma-Long History of Deformation and Magmatism from Seismic Reflection, Gravity and Magnetic Data. *Frontiers in Earth Science* **9** (2021) <https://doi.org/10.3389/feart.2021.707721>
- [20] DIGIS Team: GEOROC Compilation: Rift Volcanics (2021). <https://doi.org/10.25625/KAIVCT>
- [21] Chambers, E.L., Harmon, N., Rychert, C.A., Gallacher, R.J., Keir, D.: Imaging the seismic velocity structure of the crust and upper mantle in the northern East African Rift using Rayleigh wave tomography. *Geophysical Journal International* **230**(3), 2036–2055 (2022) <https://doi.org/10.1093/gji/ggac156>
- [22] Hanan, B.B., Graham, D.W.: Lead and Helium Isotope Evidence from Oceanic Basalts for a Common Deep Source of Mantle Plumes. *Science* **272**(5264), 991–995 (1996) <https://doi.org/10.1126/science.272.5264.991>
- [23] Hart, S.R., Hauri, E.H., Oschmann, L.A., Whitehead, J.A.: Mantle Plumes and Entrainment: Isotopic Evidence. *Science* **256**(5056), 517–520 (1992) <https://doi.org/10.1126/SCIENCE.256.5056.517>
- [24] Fitton, J.G., Saunders, A.D., Norry, M.J., Hardarson, B.S., Taylor, R.N.: Thermal and chemical structure of the Iceland plume. *Earth and Planetary Science Letters* **153**(3-4), 197–208 (1997) [https://doi.org/10.1016/S0012-821X\(97\)00170-2](https://doi.org/10.1016/S0012-821X(97)00170-2)
- [25] Benoit, M.H., Nyblade, A.A., VanDecar, J.C.: Upper mantle P-wave speed variations beneath Ethiopia and the origin of the Afar hotspot. *Geology* **34**(5), 329–332 (2006) <https://doi.org/10.1130/G22281.1>
- [26] Ritsema, J., Allen, R.M.: The elusive mantle plume. *Earth and Planetary Science Letters* **207**(1-4), 1–12 (2003) [https://doi.org/10.1016/S0012-821X\(02\)01093-2](https://doi.org/10.1016/S0012-821X(02)01093-2)

- [27] Pik, R., Marty, B., Hilton, D.R.: How many mantle plumes in Africa? The geochemical point of view. *Chemical Geology* **226**(3-4), 100–114 (2006) <https://doi.org/10.1016/j.chemgeo.2005.09.016>
- [28] Chambers, E.L., Harmon, N., Keir, D., Rychert, C.A.: Using Ambient Noise to Image the Northern East African Rift. *Geochemistry, Geophysics, Geosystems* **20**(4), 2091–2109 (2019) <https://doi.org/10.1029/2018GC008129>
- [29] Civiero, C., Armitage, J.J., Goes, S., Hammond, J.O.S.: The Seismic Signature of Upper-Mantle Plumes: Application to the Northern East African Rift. *Geochemistry, Geophysics, Geosystems* **20**(12), 6106–6122 (2019) <https://doi.org/10.1029/2019GC008636>
- [30] Gallacher, R.J., Keir, D., Harmon, N., Stuart, G., Leroy, S., Hammond, J.O.S., Kendall, J.-M., Ayele, A., Goitom, B., Ogubazghi, G., Ahmed, A.: The initiation of segmented buoyancy-driven melting during continental breakup. *Nature Communications* **7**(1), 13110 (2016) <https://doi.org/10.1038/ncomms13110>
- [31] Abouchami, W., Hofmann, A.W., Galer, S.J.G., Frey, F.A., Eisele, J., Felgenhauer, M.: Lead isotopes reveal bilateral asymmetry and vertical continuity in the Hawaiian mantle plume. *Nature* **434**(7035), 851–856 (2005) <https://doi.org/10.1038/nature03402>
- [32] Hutchison, W., Mather, T.A., Pyle, D.M., Boyce, A.J., Gleeson, M.L.M., Yirgu, G., Blundy, J.D., Ferguson, D.J., Vye-Brown, C., Millar, I.L., Sims, K.W.W., Finch, A.A.: The evolution of magma during continental rifting: New constraints from the isotopic and trace element signatures of silicic magmas from Ethiopian volcanoes. *Earth and Planetary Science Letters* **489**, 203–218 (2018) <https://doi.org/10.1016/j.epsl.2018.02.027>
- [33] Illsley-Kemp, F., Keir, D., Bull, J.M., Gernon, T.M., Ebinger, C., Ayele, A., Hammond, J.O.S., Kendall, J.M., Goitom, B., Belachew, M.: Seismicity During Continental Breakup in the Red Sea Rift of Northern Afar. *Journal of Geophysical Research: Solid Earth* **123**(3), 2345–2362 (2018) <https://doi.org/10.1002/2017JB014902>
- [34] Hofmann, A.W., Jochum, K.P., Seufert, M., White, W.M.: Nb and Pb in oceanic basalts: new constraints on mantle evolution. *Earth and Planetary Science Letters* **79**(1-2), 33–45 (1986) [https://doi.org/10.1016/0012-821X\(86\)90038-5](https://doi.org/10.1016/0012-821X(86)90038-5)
- [35] Rooney, T.O., Hanan, B.B., Graham, D.W., Furman, T., Blichert-Toft, J., Schilling, J.-G.: Upper Mantle Pollution during Afar Plume–Continental Rift Interaction. *Journal of Petrology* **53**(2), 365–389 (2012) <https://doi.org/10.1093/petrology/egr065>
- [36] Armitage, J.J., Ferguson, D.J., Goes, S., Hammond, J.O.S., Calais, E., Rychert, C.A., Harmon, N.: Upper mantle temperature and the onset of extension and

- break-up in Afar, Africa. *Earth and Planetary Science Letters* **418**, 78–90 (2015) <https://doi.org/10.1016/j.epsl.2015.02.039>
- [37] Ebinger, C.J., Sleep, N.H.: Cenozoic magmatism throughout east Africa resulting from impact of a single plume. *Nature* **395**, 788–791 (1998) <https://doi.org/10.1038/27417>
- [38] Chang, S.J., Lee, S.: Mantle plumes and associated flow beneath Arabia and East Africa. *Earth and Planetary Science Letters* **302**(3-4), 448–454 (2011) <https://doi.org/10.1016/j.epsl.2010.12.050>
- [39] Barberi, F., Varet, J.: The Erta Ale volcanic range (Danakil Depression, Northern Afar, Ethiopia). *Bulletin Volcanologique* **34**(4), 848–917 (1970) <https://doi.org/10.1007/BF02596805>
- [40] Siegburg, M., Gernon, T.M., Bull, J.M., Keir, D., Barfod, D.N., Taylor, R.N., Abebe, B., Ayele, A.: Geological evolution of the Boset-Bericha Volcanic Complex, Main Ethiopian Rift: $^{40}\text{Ar}/^{39}\text{Ar}$ evidence for episodic Pleistocene to Holocene volcanism. *Journal of Volcanology and Geothermal Research* **351**, 115–133 (2018) <https://doi.org/10.1016/j.jvolgeores.2017.12.014>
- [41] Kamber, B.S., Gladu, A.H.: Comparison of Pb Purification by Anion-Exchange Resin Methods and Assessment of Long-Term Reproducibility of Th/U/Pb Ratio Measurements by Quadrupole ICP-MS. *Geostandards and Geoanalytical Research* **33**(2), 169–181 (2009) <https://doi.org/10.1111/J.1751-908X.2009.00911.X>
- [42] Taylor, R.N., Ishizuka, O., Michalik, A., Milton, J.A., Croudace, I.W.: Evaluating the precision of Pb isotope measurement by mass spectrometry. *Journal of Analytical Atomic Spectrometry* **30**(1), 198–213 (2015) <https://doi.org/10.1039/c4ja00279b>
- [43] Pin, C., Briot, D., Bassin, C., Poitrasson, F.: Concomitant separation of strontium and samarium-neodymium for isotopic analysis in silicate samples, based on specific extraction chromatography. *Analytica Chimica Acta* **298**(2), 209–217 (1994) [https://doi.org/10.1016/0003-2670\(94\)00274-6](https://doi.org/10.1016/0003-2670(94)00274-6)
- [44] Pin, C., Zalduogui, J.S.: Sequential separation of light rare-earth elements, thorium and uranium by miniaturized extraction chromatography: Application to isotopic analyses of silicate rocks. *Analytica Chimica Acta* **339**(1-2), 79–89 (1997) [https://doi.org/10.1016/S0003-2670\(96\)00499-0](https://doi.org/10.1016/S0003-2670(96)00499-0)
- [45] Lin, F.-C., Moschetti, M.P., Ritzwoller, M.H.: Surface wave tomography of the western United States from ambient seismic noise: Rayleigh and Love wave phase velocity maps. *Geophysical Journal International* **173**(1), 281–298 (2008) <https://doi.org/10.1111/j.1365-246X.2008.03720.x>

- [46] Dziewonski, A., Landisman, M., Bloch, S., Sato, Y., Asano, S.: Progress Report on Recent Improvements in the Analysis of Surface Wave Observations. *Journal of Physics of the Earth* **16**(Special), 1–26 (1968)
- [47] Bensen, G.D., Ritzwoller, M.H., Barmin, M.P., Levshin, A.L., Lin, F., Moschetti, M.P., Shapiro, N.M., Yang, Y.: Processing seismic ambient noise data to obtain reliable broad-band surface wave dispersion measurements. *Geophysical Journal International* **169**(3), 1239–1260 (2007) <https://doi.org/10.1111/j.1365-246X.2007.03374.x>
- [48] Zhou, Y., Dahlen, F.A., Nolet, G.: Three-dimensional sensitivity kernels for surface wave observables. *Geophysical Journal International* **158**(1), 142–168 (2004) <https://doi.org/10.1111/j.1365-246X.2004.02324.x>
- [49] Harmon, N., Forsyth, D., Webb, S.: Using Ambient Seismic Noise to Determine Short-Period Phase Velocities and Shallow Shear Velocities in Young Oceanic Lithosphere. *Bulletin of the Seismological Society of America* **97**(6), 2009–2023 (2007) <https://doi.org/10.1785/0120070050>
- [50] Tarantola, A., Valette, B.: Generalized nonlinear inverse problems solved using the least squares criterion. *Reviews of Geophysics* **20**(2), 219 (1982) <https://doi.org/10.1029/RG020i002p00219>
- [51] Saito, M.: DISPER80: a subroutine package for the calculation of seismic normal-mode solutions. In: Doornbos, D.J. (ed.) *Seismological Algorithms: Computational Methods and Computer Programs*, pp. 293–319. Academic Press, ??? (1988)
- [52] Harmon, N., Rychert, C.A.: Seismic imaging of deep crustal melt sills beneath Costa Rica suggests a method for the formation of the Archean continental crust. *Earth and Planetary Science Letters* **430**, 140–148 (2015) <https://doi.org/10.1016/j.epsl.2015.07.062>
- [53] Yang, C.S., Curtis, P., Payeur, P.: Calibration of an Integrated Robotic Multi-modal Range Scanner. *IEEE Transactions on Instrumentation and Measurement* **55**(4), 1148–1159 (2006) <https://doi.org/10.1109/TIM.2006.876410>
- [54] Forsyth, D.W., Li, A.: Array analysis of two-dimensional variations in surface wave phase velocity and azimuthal anisotropy in the presence of multipathing interference, pp. 81–97 (2005). <https://doi.org/10.1029/157GM06>
- [55] Press W. H., Teukolsky S. A., Vetterling, W.T., Flannery, B.P.: *Numerical Recipes in C++: The Art of Scientific Computing*, 2nd edn. Cambridge University Press, ??? (1992)
- [56] Nishida, K.: Two-dimensional sensitivity kernels for cross-correlation functions of background surface waves. *Comptes Rendus Geoscience* **343**(8-9), 584–590 (2011)

- <https://doi.org/10.1016/j.crte.2011.02.004>
- [57] Tromp, J., Luo, Y., Hanasoge, S., Peter, D.: Noise cross-correlation sensitivity kernels. *Geophysical Journal International* **183**(2), 791–819 (2010) <https://doi.org/10.1111/j.1365-246X.2010.04721.x>
- [58] Hammond, J.O.S., Kendall, J.M., Stuart, G.W., Keir, D., Ebinger, C., Ayele, A., Belachew, M.: The nature of the crust beneath the Afar triple junction: Evidence from receiver functions. *Geochemistry, Geophysics, Geosystems* **12**(12) (2011) <https://doi.org/10.1029/2011GC003738>
- [59] Dziewonski, A.M., Anderson, D.L.: Preliminary reference Earth model. *Physics of the Earth and Planetary Interiors* **25**(4), 297–356 (1981) [https://doi.org/10.1016/0031-9201\(81\)90046-7](https://doi.org/10.1016/0031-9201(81)90046-7)
- [60] Ayele, A., Stuart, G., Kendall, J.M.: Insights into rifting from shear wave splitting and receiver functions: An example from Ethiopia. *Geophysical Journal International* **157**(1), 354–362 (2004) <https://doi.org/10.1111/j.1365-246X.2004.02206.x>
- [61] Dugda, M.T., Nyblade, A.A., Julia, J., Langston, C.A., Ammon, C.J., Simiyu, S.: Crustal structure in Ethiopia and Kenya from receiver function analysis: Implications for rift development in eastern Africa. *Journal of Geophysical Research: Solid Earth* **110**(1), 1–15 (2005) <https://doi.org/10.1029/2004JB003065>
- [62] Ogden, C.S., Bastow, I.D., Gilligan, A., Rondenay, S.: A reappraisal of the H- κ stacking technique: implications for global crustal structure. *Geophysical Journal International* **219**(3), 1491–1513 (2019) <https://doi.org/10.1093/gji/ggz364>
- [63] Stuart, G.W., Bastow, I.D., Ebinger, C.J.: Crustal structure of the northern Main Ethiopian Rift from receiver function studies. *Geological Society, London, Special Publications* **259**(1), 253–267 (2006) <https://doi.org/10.1144/GSL.SP.2006.259.01.20>
- [64] Maguire, P.K.H., Keller, G.R., Klemperer, S.L., Mackenzie, G.D., Keranen, K., Harder, S., O'Reilly, B., Thybo, H., Asfaw, L., Khan, M.A., Amha, M.: Crustal structure of the northern Main Ethiopian Rift from the EAGLE controlled-source survey; a snapshot of incipient lithospheric break-up. *Geological Society, London, Special Publications* **259**(1), 269–292 (2006) <https://doi.org/10.1144/GSL.SP.2006.259.01.21>
- [65] Keranen, K.M., Klemperer, S.L., Julia, J., Lawrence, J.F., Nyblade, A.A.: Low lower crustal velocity across Ethiopia: Is the Main Ethiopian Rift a narrow rift in a hot craton? *Geochemistry, Geophysics, Geosystems* **10**(5), (2009) <https://doi.org/10.1029/2008GC002293>

- [66] Eilers, P.H.C., Marx, B.D.: Flexible smoothing with B-splines and penalties. *Statistical Science* **11**(2) (1996) <https://doi.org/10.1214/ss/1038425655>
- [67] Eilers, P.H.C., Marx, B.D.: Splines, knots, and penalties. *Wiley Interdisciplinary Reviews: Computational Statistics* **2**(6), 637–653 (2010) <https://doi.org/10.1002/wics.125>
- [68] Boor, C.: *A Practical Guide to Splines* vol. 27. Springer, New York, NY (2001). <https://doi.org/10.1007/978-1-4612-6333-3>
- [69] Jones, M., Randell, D., Ewans, K., Jonathan, P.: Statistics of extreme ocean environments: Non-stationary inference for directionality and other covariate effects. *Ocean Engineering* **119**, 30–46 (2016) <https://doi.org/10.1016/j.oceaneng.2016.04.010>
- [70] Arthur, D., Vassilvitskii, S.: K-means++ the advantages of careful seeding. In: Eighteenth Annual ACM-SIAM Symposium on Discrete Algorithms, pp. 1027–1035 (2007). <https://doi.org/10.5555/1283383>
- [71] McDonough, W.F., Sun, S.-s.: The composition of the Earth. *Chemical Geology* **120**(3-4), 223–253 (1995) [https://doi.org/10.1016/0009-2541\(94\)00140-4](https://doi.org/10.1016/0009-2541(94)00140-4)
- [72] Stracke, A., Hofmann, A.W., Hart, S.R.: FOZO, HIMU, and the rest of the mantle zoo. *Geochemistry, Geophysics, Geosystems* **6**(5) (2005) <https://doi.org/10.1029/2004GC000824>
- [73] Zindler, A., Hart, S.: Chemical Geodynamics. *Annual Review of Earth and Planetary Sciences* **14**(1), 493–571 (1986) <https://doi.org/10.1146/annurev.ea.14.050186.002425>
- [74] Hart, S.R.: Heterogeneous mantle domains: signatures, genesis and mixing chronologies. *Earth and Planetary Science Letters* **90**(3), 273–296 (1988) [https://doi.org/10.1016/0012-821X\(88\)90131-8](https://doi.org/10.1016/0012-821X(88)90131-8)